Supporting Information

Tuning Energy Landscapes and Metal-Metal Interactions in Supramolecular Polymers regulated by Coordination Geometry

Nils Bäumer,[a] Kalathil K. Kartha,[a] Stefan Buss,[b] Iván Maisuls,[b] Jasnamol P. Palakkal,[c] Cristian A. Strassert,[b] Gustavo Fernández*[a]

[a]Organisch-Chemisches Institut, Universität Münster, Corrensstraße 40, 48149 Münster, Germany.

[b]CiMIC, SoN, Institut für Anorganische und Analytische Chemie, Westfälische Wilhelms-Universität Münster, Corrensstraße 28/30, 48149 Münster, Germany; CeNTech, Westfälische Wilhelms-Universität Münster, Heisenbergstraße 11, 48149 Münster, Germany.

[c]Technische Universität Darmstadt, Department of Materials and Earth Sciences, Alarich-Weiss-Straße 2, 64287 Darmstadt, Germany.

Table of Contents

1. Materials and Methods

General Procedures: All solvents were dried according to standard procedures. Reagents were used as purchased. All air-sensitive reactions were carried out under argon atmosphere.

NMR measurements: ^{1}H and ^{13}C NMR spectra were recorded on a Bruker Avance 400 (^{1}H: 400 MHz; ^{13}C: 100.6 MHz) and a Bruker AV300 (^{1}H: 300 MHz; ^{13}C: 100.6 MHz). Additional 1D ^{1}H as well as 2D H,H COSY and 2D H,H ROESY spectra were recorded on an Agilent DD2 500 (^{1}H: 500 MHz) and an Agilent DD2 600 (^{1}H: 600 MHz) at a standard temperature of 298 K in deuterated solvents. Deviating temperature is explicitly mentioned when used. The recorded spectra were referenced to the remaining resonance signals of the deuterated solvents ($CDCl_3$: 7.26 ppm (^{1}H); DCM: 5.32 ppm (^{1}H)). The coupling constant J of the measured spin multiplets is given in Hertz (Hz) and the chemical shifts are given in reference to the chemical shift of trimethylsilane (0 ppm). The abbreviations used to analyze the recorded spectra are: s (singlet), d (doublet), m (multiplet).

Mass spectroscopy: MALDI-mass spectra were recorded on an Autoflex Speed manufactured by Bruker Daltronics. A SmartBeamTM NdYAF-Laser with a wavelength of 335 nm was used. The signals are described by their mass/charge ratio (m/z) in u.

UV-Vis spectroscopy: All UV-Vis spectra were recorded on a V-770 and a V-750 by the company JASCO with a spectral bandwidth of 1.0 nm and a scan rate of 400 nm min^{-1}. Glass cuvettes with an optical length of 1 cm and 1 mm were used. All measurements have been conducted in solvents from commercial sources of spectroscopic grade.

Atomic force microscopy: The AFM images have been recorded on a Multimode®8 SPM Systems manufactured by Bruker AXS. The used cantilevers were AC200TS by Oxford Instruments with an average spring constant of 9 N m^{-1}, an average frequency of 150 kHz, an average length of 200 µm, an average width of 40 µm and an average tip radius of 7 nm. All solutions have been spin-coated onto an HOPG surface using a spin rate between 2000 and 4000 rpm.

Fluorescence spectroscopy: All fluorescence spectra were recorded on a JASCO FP-8500 spectrofluorometer. Glass cuvettes with an optical length of 1 cm were used. All measurements have been conducted in solvents from commercial sources of spectroscopic grade.

Lifetime measurements: Steady-state excitation and emission spectra were recorded on a FluoTime300 spectrometer from PicoQuant equipped with a 300 W ozone-free Xe lamp (250-900 nm), a 10 W Xe flash-lamp (250-900 nm, pulse width < 10 µs) with repetition rates of 0.1 – 300 Hz, an excitation monochromator (Czerny-Turner 2.7 nm/mm dispersion, 1200 grooves/mm, blazed at 300 nm), diode lasers (pulse width < 80 ps) operated by a computer-controlled laser driver PDL-820 (repetition rate up to 80 MHz, burst mode for slow and weak decays), two emission monochromators (Czerny-Turner, selectable gratings blazed at 500 nm with 2.7 nm/mm dispersion and 1200 grooves/mm, or blazed at 1250 nm with 5.4 nm/mm dispersion and 600 grooves/mm), Glan-Thompson polarizers for excitation (Xe-lamps) and emission, a Peltier-thermostatized sample holder from Quantum Northwest (-40 °C – 105 °C), and two detectors, namely a PMA Hybrid 40 (transit time spread FWHM < 120 ps, 300 – 720 nm) and a R5509-42 NIR-photomultiplier tube (transit time spread FWHM 1.5 ns, 300-1400 nm) with external cooling (-80 °C) from Hamamatsu. Steady-state and fluorescence lifetimes were recorded in TCSPC mode by a PicoHarp 300 (minimum base resolution 4 ps). Phosphorescence lifetimes were recorded in MCS mode by a NanoHarp 250 (minimum base resolution 4 ns). Burst mode was used to obtain longer lifetimes, where the diode laser first emits a variable number of laser pulses at repetition rates in the MHz range and is then switched off to detect the emission of the sample, where the individual laser pulses act like one single pulse with a much higher pulse energy. The number of pulses (and consequently the total time of the excitation burst) was adapted to the luminescence intensity of each sample, as weak emitters will require a longer train of excitation pulses. Emission and excitation spectra were corrected for source intensity (lamp and grating) by standard correction curves. Lifetime analysis was performed using the commercial FluoFit software. The quality of the fit was assessed by minimizing the reduced chi squared function ($\chi 2$) and visual inspection of the weighted residuals and their autocorrelation. Luminescence quantum yields were measured with a Hamamatsu Photonics absolute PL quantum yield measurement system (C9920-02) equipped with a L9799-01 CW Xenon light source (150 W), monochromator, C7473 photonic multi-channel analyzer, integrating sphere and employing U6039-05 PLQY measurement software (Hamamatsu Photonics, Ltd., Shizuoka,

Japan). All samples were measured in Suprasil® quartz cuvettes with septa. Deaerated samples were measured upon flushing with argon for 20 min (using the septa with a cannula).

XRD diffraction analysis: Powder XRD diffraction experiments have been conducted on a ®Rigaku Smartlab X-ray diffractometer in parallel beam geometry with Cu-Kα radiation. The measurement steps were 0.01 deg with a measurement time per step of 0.6 s, using a voltage of 45 kV and a current of 190 mA. Samples have been prepared by stepwise dropcasting a solution with a concentration of 7.5 mM onto a glass microscope plate from FisherbrandTM with a thickness of 0.8-1 mm.

Scanning Electron Microscopy: The SEM images have been recorded on a Phenom Pharos Desktop SEM and on a Phenom ProX Desktop SEM manufactured by Thermo Fisher Scientific. The individual images have been recorded using a zoom between 22500x and 300x with either a BSD or SED detector and an acceleration voltage of either 5 or 10 kV (For individual images please see the corresponding figure caption). All solutions have been dropcasted onto a silicon wafer (10 µL) and additionally coated with Pt using a physical vapor deposition for a time interval of 30 seconds prior to measurement.

Fluorescence Microscopy: Photoluminescence images were acquired using a Fluorescence Microscopy (MicroTime 200, Picoquant®), using as excitation source a λ=375nm Xe lamp with BP360-370 and BA520IF filters.

Nano AFM-IR: Photothermal AFM-IR measurements were performed on a nanoIR3-s system (Anasys Instruments/Bruker Nano Surfaces Division, Santa Barbara (CA), USA) equipped with an OPO laser in the higher wavenumber range (3600-2700 cm^{-1}). Sample investigations were done in resonance enhanced AFM-IR mode (contact), where the laser pulse rate is tuned to one of the cantilever contact resonant frequencies (here approx. 295 kHz). Photothermal AFM-IR spectra were collected in the 3600-2700 wavenumber range with 4 cm^{-1} spectral resolution and approx. 4 % laser power. Probe: Gold-coated Si-Probe. Resonance frequency ~ 75 kHz, spring constant ~1-7 N/m and tip radius < 25 nm.

PF-TUNA measurements: PF-TUNA measurements were conducted on a Dimension Icon XR SPM system (Bruker, Nano Surfaces Division, Santa Barbara (CA), USA), placed in an acoustic hood with integrated passive, air-damped vibration isolation table and faradaic shielding. Probe: SCM-PIT, PtIr coated soft tapping probe, spring constant 2.8N/m, resonance frequency 75kHz, tip radius 25nm. Modes: PeakForce TUNA, ultrafast force-distance curves, with feedback-controlled loading force of 12nN (peak force setpoint), 1kHz sinusoidal z modulation with selected 20-50nm amplitude, bias 5V, current sensitivity (PeakForce TUNA module) of 1nA/V. Current during contact time, point of maximum load and average during whole 1kHz cycle was monitored besides topography, adhesion force and modulus, pixel resolution 512x512, scan size 10 m, scan rate 0.27Hz. Datacube TUNA: Fast Force Volume based mapping mode, using segmented force-distance curves at each pixel with approach, feedback controlled holding segment (allowing to perform an IV-sweep) and retract. z Ramp Size 300nm, loading force 25nN (relative deflection trigger), ramp frequency 61Hz (loading/unloading speed 36um/s), holding time of 200ms at 25nN, bias sweep from -5V to +5V. Map size 5um x 5um, 64x64 pixel (producing 2 Datacubes based on 4096 force-distance curves and co-located 4096 I-V-curves). From the datacubes, co-located topographic, mechanical, and current maps can be calculated.

FT-IR spectroscopy measurements: Thin film measurements were carried out using a *JASCO-FT-IR-6800* equipped with a CaF_2 window. Thin films were prepared by dropcasting 200 µL of the respective solutions in MCH with a concentration of 1 x 10^{-3} M.

2. Synthetic details and characterization

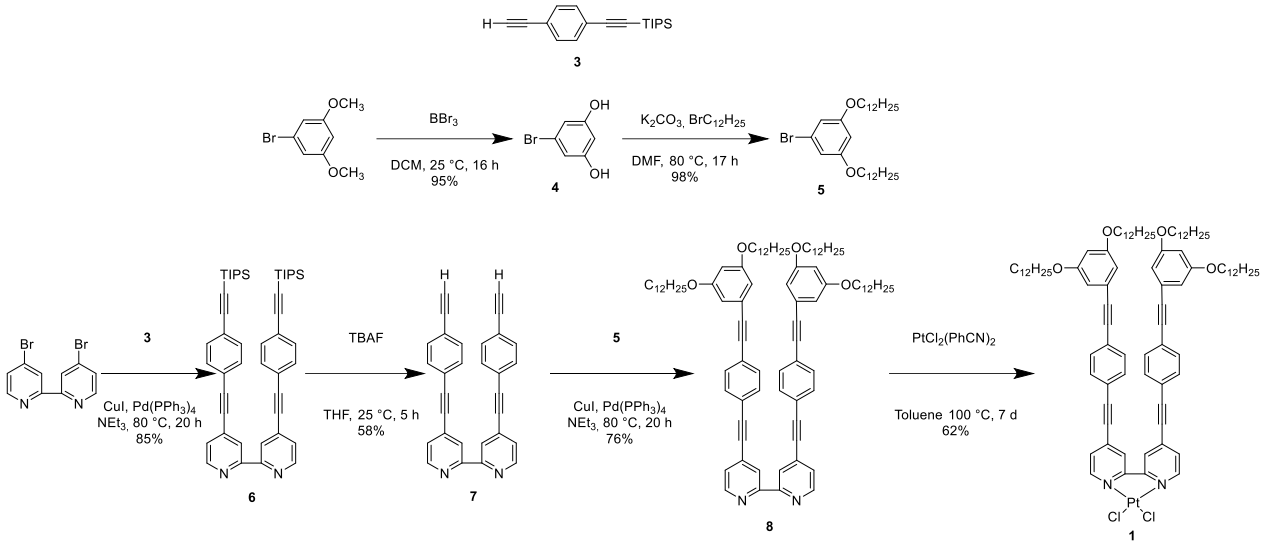

Scheme S1. Synthesis of complex **1**.

Molecule **3** was synthesized according to a procedure previously reported by our group.[1]

Synthesis of **4**

4 was synthesized according to a previously reported method.[2] 1-Bromo-3,5-dimethoxybenzene (2.05 g, 9.46 mmol, 1.0 eq.) was dissolved in DMF (30 mL) and cooled to 0 °C. BBr3 (2.5 ml, 6.6 g, 26 mmol, 2.8 eq.) was added dropwise. The ice bath was removed and the solution stirred at 25 °C for 16 h. The crude product was poured on ice and the aqueous solution extracted with EtOAc (3 x 20 mL). The combined organic phases were washed with brine and dried over $MgSO_4$. The solvent was removed in vacuo and the product was obtained as a brown solid.

Yield: 1.70 g, 9.02 mmol, 95%

^{1}H NMR (300 MHz, $CDCl_3$, 298 K): δ = 6.60 (d, J = 2.2 Hz, 2H); 6.29 (t, J = 2.2 Hz, 1H); 5.22 (s, 2H) ppm.

Synthesis of **5**

5 was synthesized according to a previously reported method.[3] 1-Bromo-3,5-dihydroxybenzene (1.07 g, 5.67 mmol, 1.0 eq.) and K_2CO_3 (3.14 g, 13.6 mmol, 2.4 eq.) were dissolved in dried, degassed DMF (25 mL). Dodecyl bromide (3.40 mL, 3.54 g, 22.7 mmol, 4.0 eq.) was added dropwise. The solution was stirred at 80 °C for 17 h. The solvent was removed in vacuo and the residue dissolved in EtOAc (20 mL). The organic phase was washed with water and brine (2 x 10 mL each) and dried over $MgSO_4$. The solvent was removed and the crude product purified by column chromatography (SiO_2, DCM/pentane (2:98)). The product was obtained as a white solid.

Yield: 2.91 g, 5.54 mmol, 98%

^{1}H NMR (300 MHz, $CDCl_3$, 298 K): δ = 6.63 (d, J = 2.2 Hz, 2H); 6.36 (t, J = 2.2 Hz, 1H); 3.89 (t, J = 6.5 Hz, 4H); 1.80-1.68 (m, 4H); 1.45-1.38 (m, 4H); 1.36-1.20 (m, 32H); 0.91-0.84 (m, 6H) ppm.

Synthesis of **6**

4,4'-Dibromo-2,2'-bipyridine (638 mg, 2.03 mmol, 1.0 eq.), $Pd(PPh_3)_4$ (240 mg, 0.2 mmol, 0.1 eq.) and CuI (15 mg, 0.08 mmol, 0.04 eq.) were dissolved in degassed NEt_3 (20 mL) and stirred at 25 °C for 30 min. Afterwards, **3** (1.28 g, 4.5 mmol, 2.2 eq.) dissolved in degassed NEt_3 (8 mL) was added dropwise and the solution was stirred at 80 °C for 20 h. The solvent was removed in vacuo and the crude product purified by column chromatography (SiO_2, DCM/ pentane (1:1)) yielding a white powder.

Yield: 1.24 g, 1.73 mmol, 85%

^{1}H NMR (400 MHz, $CDCl_3$, 298 K): δ = 8.70 (d, J = 4.9 Hz, 2H), 8.57 (s, 2H), 7.53-7.47 (m, 8H), 7.43 (d, J = 4.9 Hz, 2H), 1.19-1.09 (m, 42H).

^{13}C NMR (100.6 MHz, $CDCl_3$, 298 K): δ = 155.06, 149.10, 133.01, 132.25, 131.91, 125.84, 124.64, 123.73, 121.97, 106.54, 94.45, 93.80, 88.64, 18.81, 11.45 ppm.

HRMS (ESI in MeOH) m/z: Calculated: 717.40548 $[M+H]^+$; Found: 717.40532.

Synthesis of **7**

6 (725 mg, 1.01 mmol, 1.0 eq.) was dissolved in THF (30 mL) and stirred at 25 °C. TBAF (1 M in THF, 2.5 mL, 2.5 mmol, 1.3 eq.) was added dropwise and the solution was stirred for 5 h at 25 °C. The solvent was evaporated and the residue was dissolved in DCM, washed with water (3 x 10 mL) and brine (10 mL) and dried over $MgSO_4$. The solvent was removed in vacuo and the crude product purified by column chromatography (SiO_2, DCM/MeOH (99:1)), yielding a white powder.

Yield: 237 mg, 0.058 mmol, 58%

^{1}H NMR (400 MHz, DMF-d_7, 298 K): δ = 8.85 (dd, J = 5.0, 0.9 Hz, 2H), 8.57 (dd, J = 1.6, 0.9 Hz, 2H), 7.79-7.74 (m, 4H), 7.70 (dd, J = 5.0, 1.6 Hz, 2H), 7.68-7.63 (m, 4H), 4.39 (s, 2H) ppm.

^{13}C NMR (100.6 MHz, DMF-d_7, 298 K): δ = 156.50, 151.16, 133.42, 133.31, 132.75, 127.04, 124.46, 123.31, 123.25, 94.24, 89.66, 84.00, 83.35 ppm.

HRMS (ESI in MeOH/$CHCl_3$) m/z: Calculated: 405.1386 $[M+H]^+$; Found: 405.1383.

Synthesis of **8**

7 (150 mg, 0.37 mmol, 1.0 eq.), **5** (465 mg, 0.89 mmol, 2.4 eq.), $Pd(PPh_3)_4$ (42 mg, 0.09 mmol, 0.2 eq.) and CuI (2 mg, 0.01 mmol, 0.03 eq.) were dissolved in degassed NEt_3 (15 mL) and stirred at 25 °C for 30 min. Afterwards, the solution was stirred at 80 °C for 20 h. The solvent was evaporated and the crude product was purified by column chromatography (SiO_2, DCM/pentane (1:3)) yielding a white solid.

Yield: 363 mg, 0.28 mmol, 76%

^{1}H NMR (400 MHz, $CDCl_3$, 298 K): δ = 8.70 (d, J = 5.0 Hz, 2H); 8.58-8.53 (m, 2H); 7.54 (s, 8H); 7.42 (d, J = 5.0 Hz, 2H); 6.68 (d, J = 2.2 Hz, 4H); 6.47 (t, J = 2.2 Hz, 2H); 3.95 (t, J = 6.5 Hz, 8H); 1.83-1.73 (m, 8H); 1.51-1.41 (m, 8H); 1.39-1.21 (m, 64H); 0.91-0.85 (m, 12H) ppm.

^{13}C NMR (100.6 MHz, $CDCl_3$, 298 K): δ = 160.27, 155.00, 149.06, 132.06, 131.84, 131.82, 128.56, 125.89, 124.43, 124.08, 123.75, 121.90, 110.07, 103.24, 92.28, 88.67, 88.34, 68.37, 32.07, 29.82, 29.79, 29.75, 29.73, 29.52, 29.50, 29.35, 26.17, 22.84, 14.27 ppm.

HRMS (ESI in MeOH) m/z: Calculated: 1293.93209 $[M+H]^+$; Found: 1293.93213.

Synthesis of **1**

8 (50 mg, 0.039 mmol, 1.0 eq.) and $PtCl_2(PhCN)_2$ (18 mg, 0.039 mmol, 1.0 eq.) were dissolved in distilled toluene (5 mL) under Argon and stirred at 100 °C for 7 days. The solvent was removed and the crude product purified by column chromatography (SiO_2, DCM), yielding the product as an orange solid.

Yield: 37 mg, 0.024 mmol, 62%

^{1}H NMR (400 MHz, $CDCl_3$, 298 K): δ = 9.50 (d, J = 6.1 Hz, 2H); 8.02 (s, 2H); 7.58-7.51 (m, 6H); 7.47 (d, J = 7.9 Hz, 4H); 6.64 (d, J = 2.2 Hz, 4H); 6.45 (t, J = 2.2 Hz, 2H); 3.93 (t, J = 6.5 Hz, 8H); 1.80-1.72 (m, 8H); 1.48-1.40 (m, 8H); 1.37-1.25 (m, 64H); 0.91-0.86 (m, 12H) ppm.

^{13}C NMR (100.6 MHz, $CDCl_3$, 298 K): δ = 160.26, 156.39, 148.89, 134.81, 132.43, 131.85, 128.76, 125.42, 125.36, 123.86, 120.70, 110.09, 103.23, 99.98, 93.14, 88.19, 87.75, 68.36, 32.07, 29.82, 29.79, 29.77, 29.74, 29.56, 29.50, 29.37, 26.19, 22.84, 14.26 ppm.

HRMS (ESI in MeOH/CHCl3 + DCTB) m/z: Calculated: 1581.81739 $[M+Na]^+$; Found: 1581.81927.

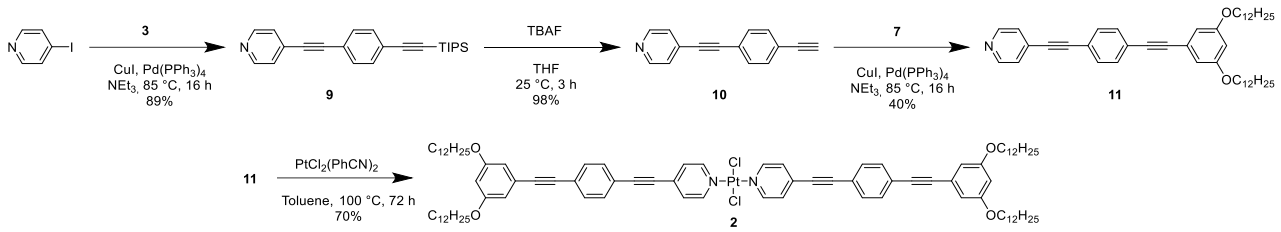

Scheme S2. Synthesis of complex **2**.

Synthesis of **9**

9 was synthesized according to a previously reported procedure.[6] $Pd(PPh_3)_4$ (57.8 mg, 0.05 mmol, 0.05 eq.), CuI (5.6 mg, 0.03 mmol, 0.03 eq.) and 4-Iodopyridine (205.3 mg, 1.00 mmol, 1.0 eq.) were dissolved in freshly degassed NEt_3 (10 mL) under argon atmosphere and stirred for 20 min. at room temperature. Subsequently, **3** (311.1 mg, 1.10 mmol, 1.1 eq.) was added and the reaction mixture was stirred at 85 °C for 16 h. The solvent was evaporated and the crude product was purified by column chromatography (DCM/methanol 98:2), yielding a white powder.

Yield: 319.6 mg, 0.89 mmol, 89 %.

^{1}H NMR (300 MHz, $CDCl_3$): δ (ppm) = 8.70 (s, 2H); 7.49 (s, 4H); 7.43 (s, 2H); 1.14 (m, 21H) ppm.

Synthesis of **10**

10 was synthesized according to a previously reported procedure.[6] **9** (319.6 mg, 0.89 mmol, 1.0 eq.) was dissolved in THF (30 mL) and TBAF (1M in THF) (1.07 mL, 1.07 mmol, 1.2 eq.) was added dropwise while stirring. The mixture was stirred at room temperature for 3 h. The solvent was removed under reduced pressure and the residue was dissolved in DCM (25 mL). The organic phase was washed with water (4 x 10 mL) and brine (10 mL) and dried over $MgSO_4$. The solvent was evaporated and the crude product purified by column chromatography (DCM). The product was obtained as a white powder.

Yield: 176.5 mg, 0.87 mmol, 98 %.

^{1}H NMR (300 MHz, $CDCl_3$): δ (ppm) = 8.55 (d, J = 5.1 Hz, 2H); 7.45 (s, 4H); 7.35 (d, J = 5.1 Hz, 2H); 3.18 (s, 1H) ppm.

Synthesis of **11**

$Pd(PPh_3)_4$ (90 mg, 0.08 mmol, 0.05 eq.), CuI (9 mg, 0.05 mmol, 0.03 eq.) and **5** (820 mg, 1.56 mmol, 1.0 eq.) were dissolved in freshly degassed NEt_3 (5 mL) under argon atmosphere and stirred for 20 min. at room temperature. Afterwards, **10** (317 mg, 1.56 mmol, 1.0 eq.) dissolved in NEt_3 (1 mL) was added and the solution was stirred at 85 °C for 16 h. The solvent was removed and the crude product purified by column chromatography (DCM/methanol 98:2), yielding a white powder.

Yield: 375 mg, 0.63 mmol, 40%.

^{1}H NMR (400 MHz, $CDCl_3$, 298 K): δ = 8.71 (s, 2H), 7.52 (s, 4H), 7.42 (s, 2H), 6.67 (d, J = 2.3 Hz, 2H), 6.47 (t, J = 2.3 Hz, 1H), 3.94 (t, J = 6.5 Hz, 4H), 1.85 – 1.73 (m, 4H), 1.49 – 1.40 (m, 4H), 1.37 – 1.20 (m, 32H), 0.95 – 0.84 (m, 6H) ppm.

^{13}C NMR (100.6 MHz, $CDCl_3$, 298 K): δ = 160.13, 149.71, 131.81, 131.68, 131.14, 124.18, 123.91, 121.79, 109.91, 103.07, 93.55, 92.07, 88.38, 88.16, 77.23, 68.22, 53.42, 31.93, 29.68, 29.65, 29.61, 29.59, 29.38, 29.37, 29.21, 26.03, 22.70, 14.13 ppm.

Micro-TOF-ESI (MeOH): calculated: 648.4702 $[M+H]^+$, found: 648.4769.

Synthesis of **2**

11 (150 mg, 0.23 mmol, 2.1 eq.) and $PtCl_2(PhCN)_2$ (55 mg, 0.11 mmol, 1.0 eq.) were dissolved in dried toluene (10 mL) and stirred at 100 °C for 72 h. The solvent was removed and the crude product purified by column chromatography (DCM). Minor impurities that could not be removed by column chromatography were removed by precipitation from DCM with diethylether. The product was obtained as pale-yellow powder.

Yield: 126 mg, 0.08 mmol, 70%.

^{1}H NMR (400 MHz, $CDCl_3$, 298 K): δ = 8.87 (d, J = 7.0 Hz, 2H); 7.54 (s, 4H); 7.36 (d, J = 7.0 Hz, 2H); 6.67 (d, J = 2.3 Hz, 2H); 6.48 (t, J = 2.3 Hz, 1H); 3.94 (t, J = 6.6 Hz, 4H); 1.82 – 1.72 (m, 4H); 1.49 – 1.39 (m, 4H); 1.38 – 1.20 (m, 32H); 0.88 (t, J = 6.7 Hz, 6H) ppm.

^{13}C NMR (100.6 MHz, $CDCl_3$, 298 K): δ = 160.14, 153.20, 134.00, 132.08, 131.77, 126.93, 125.01, 123.79, 120.85, 109.94, 103.16, 97.90, 92.60, 88.04, 87.03, 77.35, 77.03, 76.71, 68.23, 31.93, 29.68, 29.65, 29.62, 29.59, 29.38, 29.37, 29.20, 26.03, 22.71, 14.14 ppm.

HRMS (ESI in MeOH/CHCl3 + DCTB) m/z: Calculated: 1583.83304 $[M+Na]^+$; Found: 1583.83449.

3. Collection of NMR Spectra

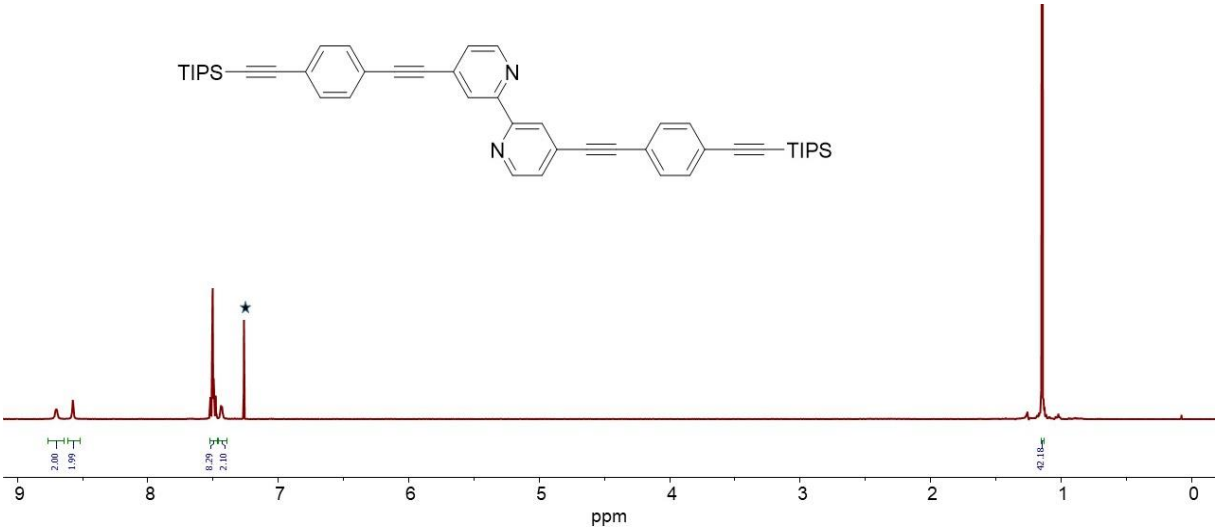

Figure S1: ^{1}H NMR spectrum of **6** (400 MHz, $CDCl_3$, 298 K).

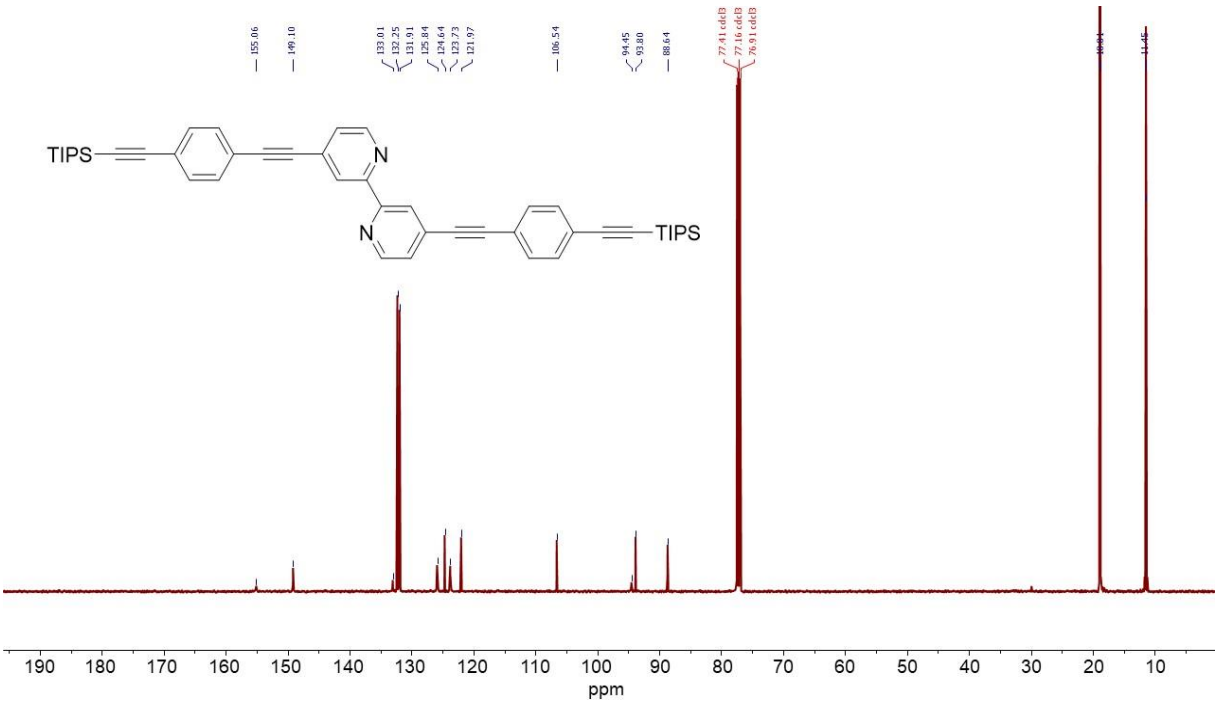

Figure S2: ^{13}C NMR spectrum of **6** (100.6 MHz, $CDCl_3$, 298 K).

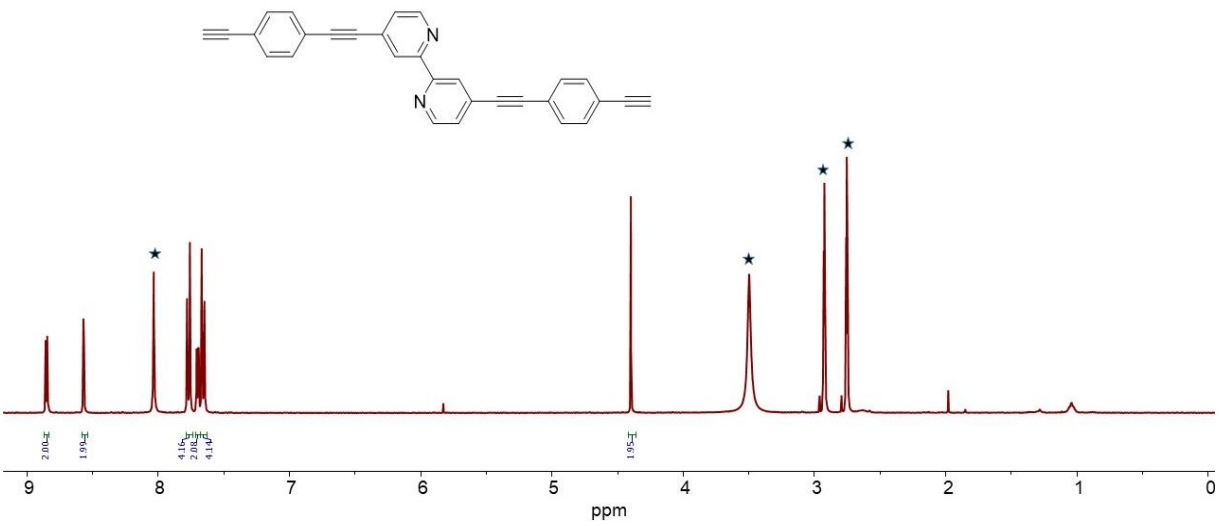

Figure S3: ^{1}H NMR spectrum of **7** (400 MHz, DMF-d_7, 298 K).

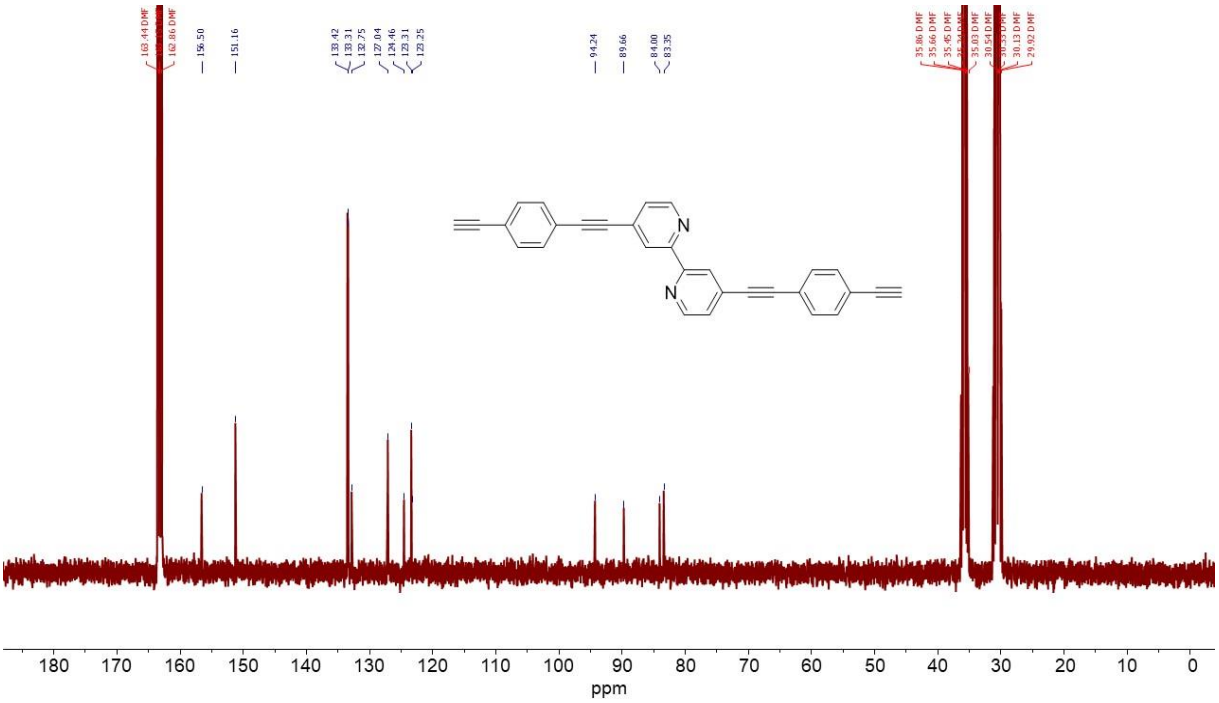

Figure S4: ^{13}C NMR spectrum of **7** (100.6 MHz, DMF-d_7, 298 K).

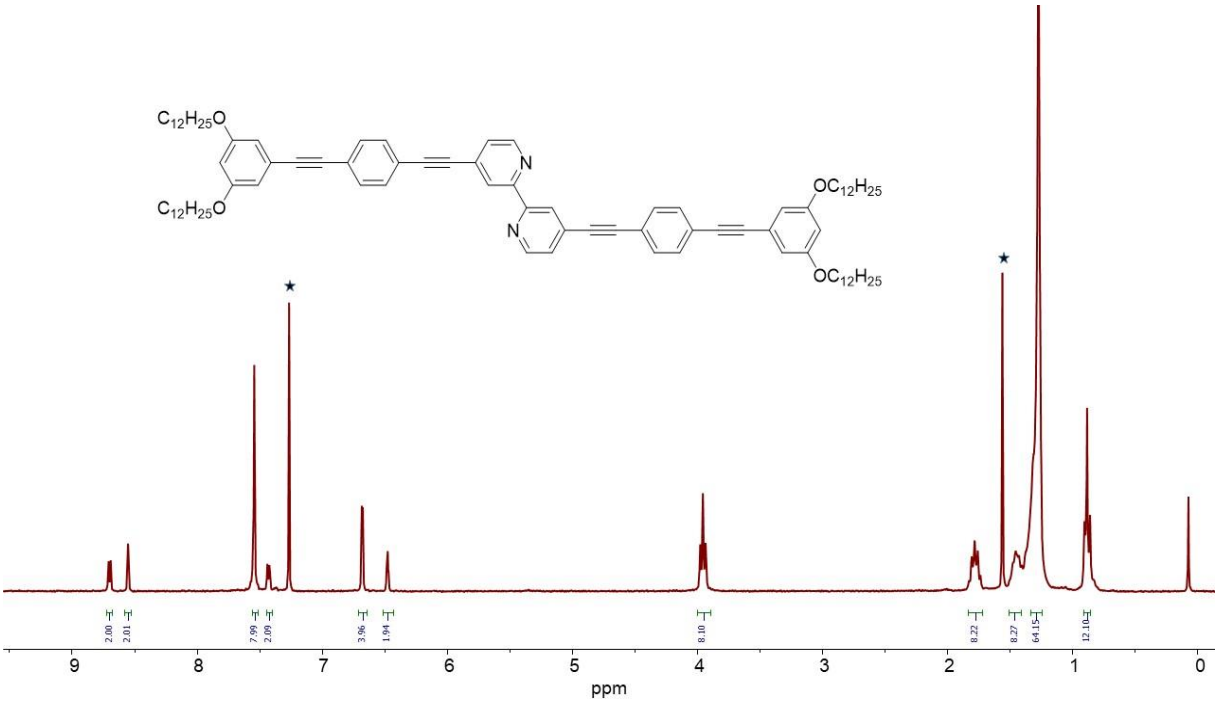

Figure S5: ^{1}H NMR spectrum of **8** (400 MHz, $CDCl_3$, 298 K).

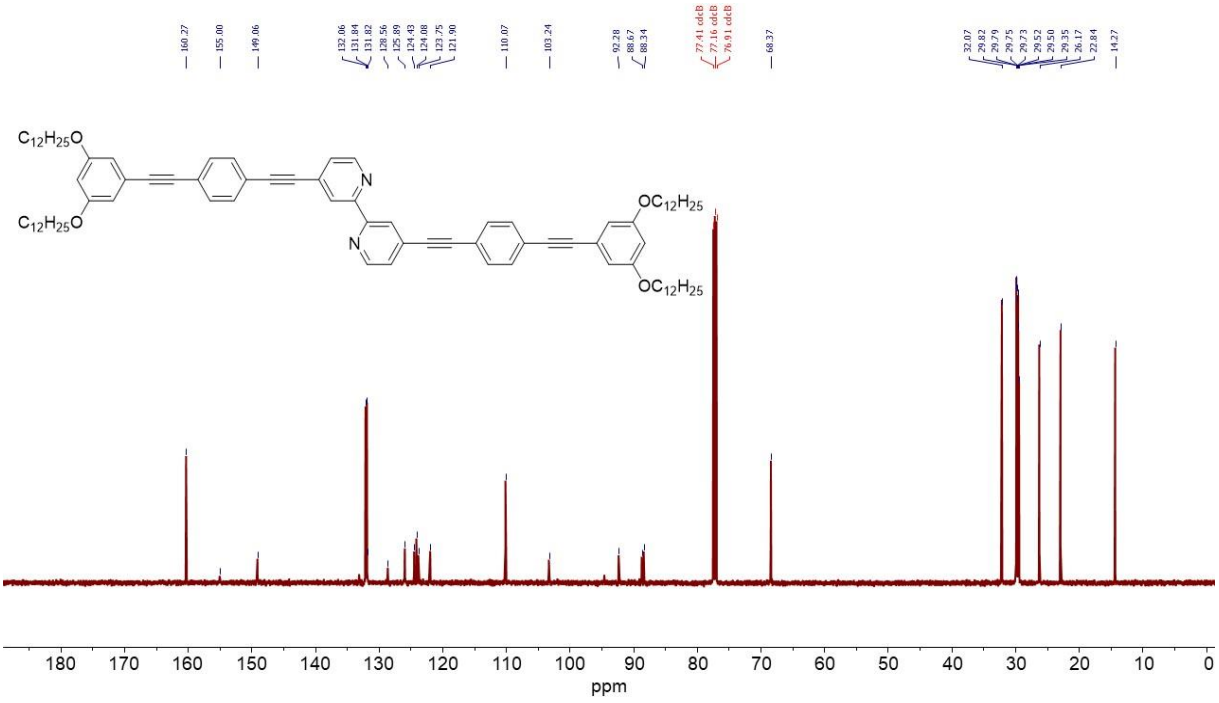

Figure S6: ^{13}C NMR spectrum of **8** (100.6 MHz, $CDCl_3$, 298 K).

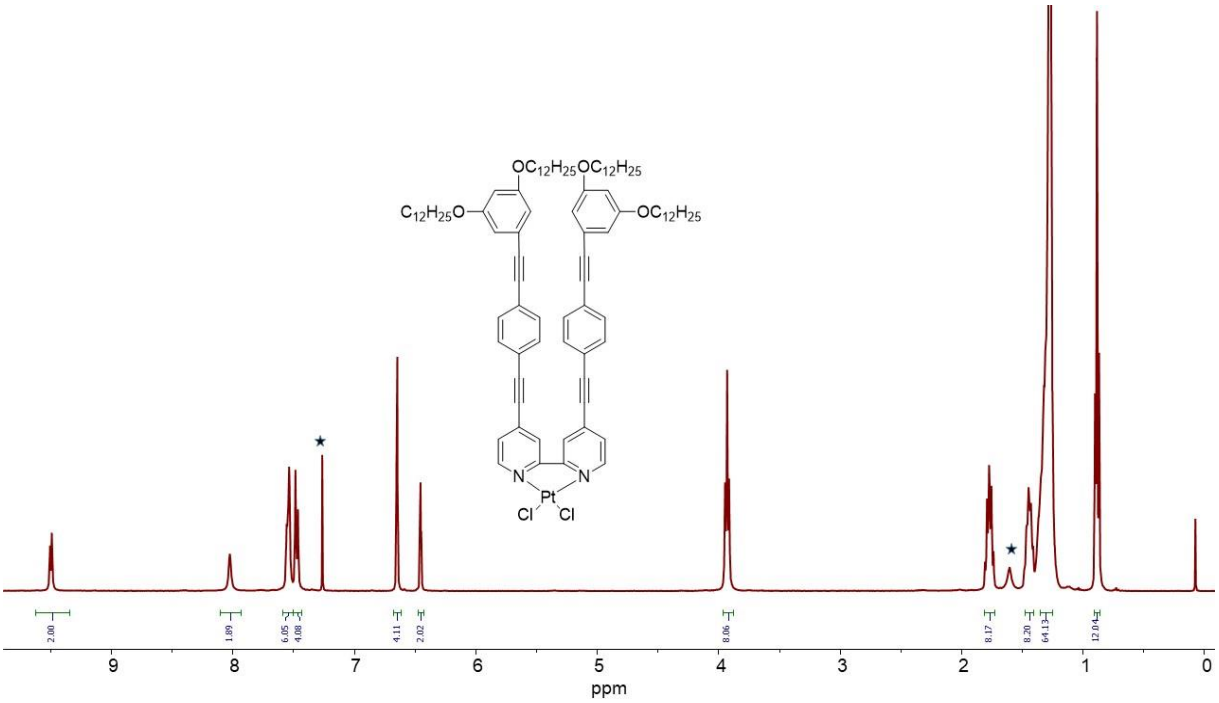

Figure S7: ^{1}H NMR spectrum of **1** (400 MHz, $CDCl_3$, 298 K).

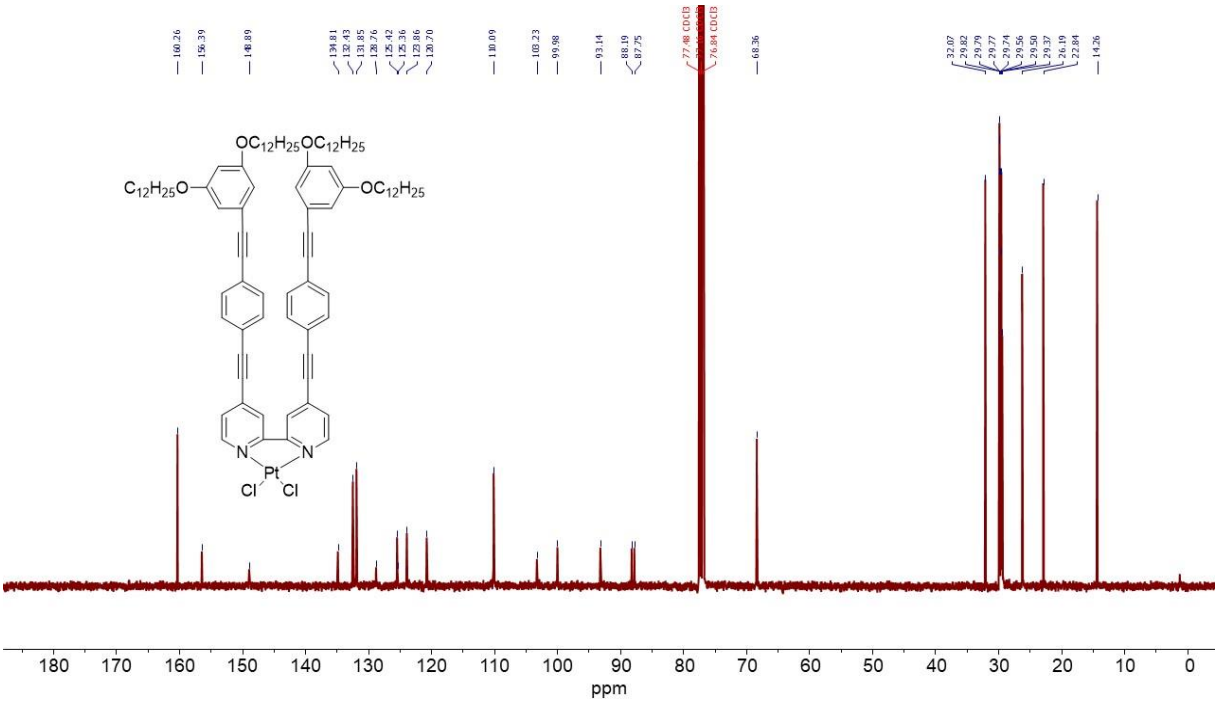

Figure S8: ^{13}C NMR spectrum of **1** (100.6 MHz, $CDCl_3$, 298 K).

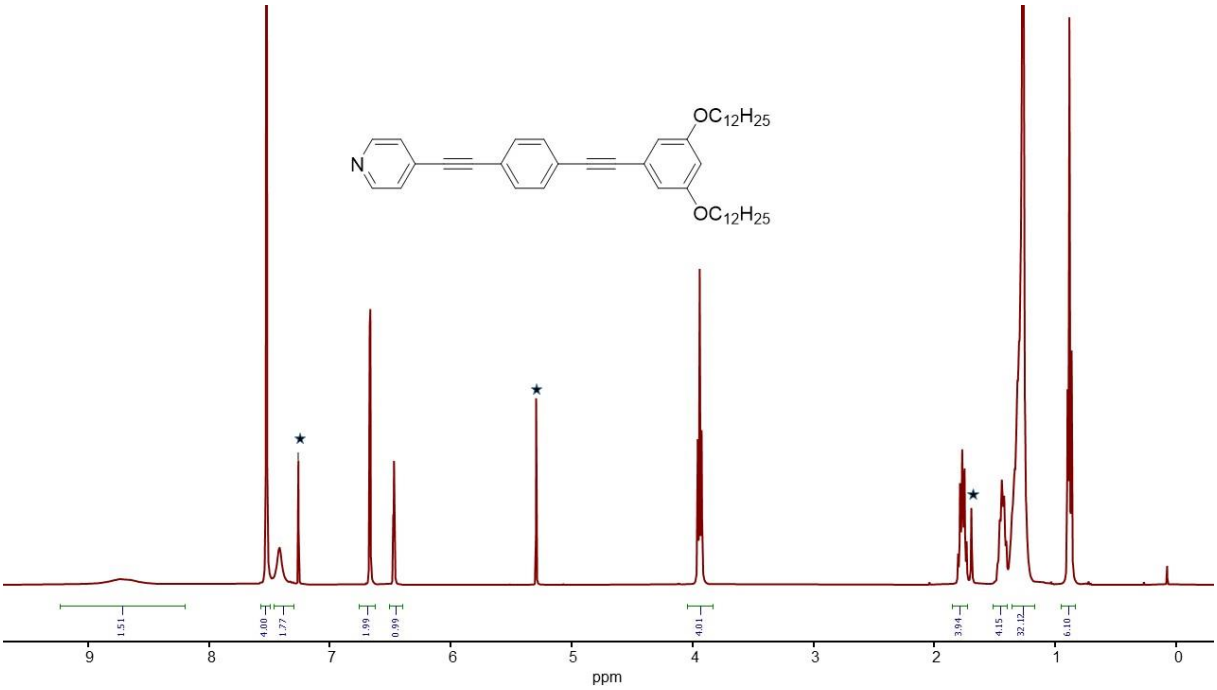

Figure S9: ^{1}H NMR spectrum of **11** (400 MHz, $CDCl_3$, 298 K).

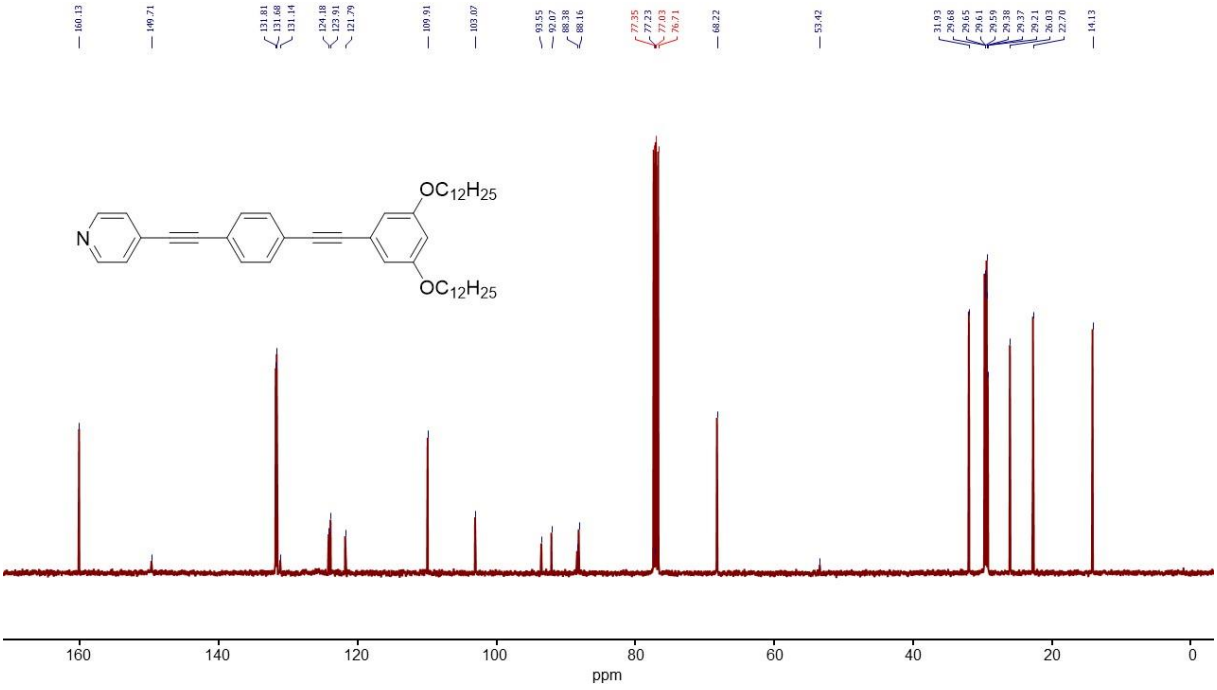

Figure S10: ^{13}C NMR spectrum of **11** (100.6 MHz, $CDCl_3$, 298 K).

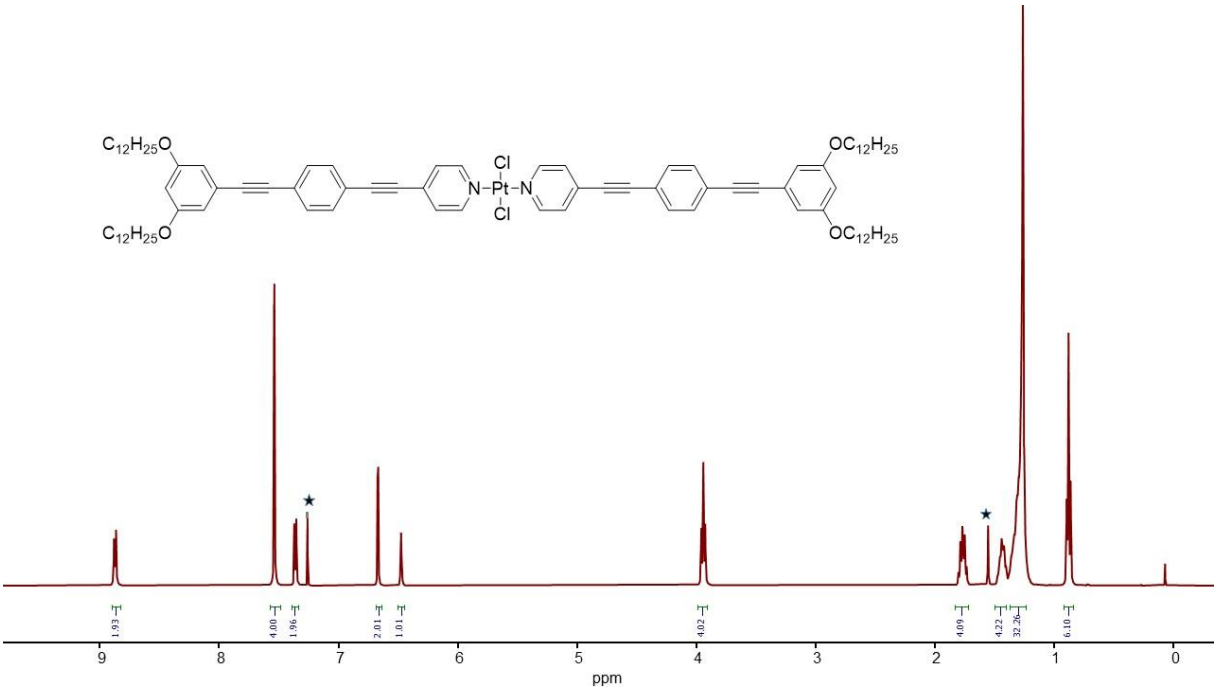

Figure S11: ^{1}H NMR spectrum of **2** (400 MHz, $CDCl_3$, 298 K).

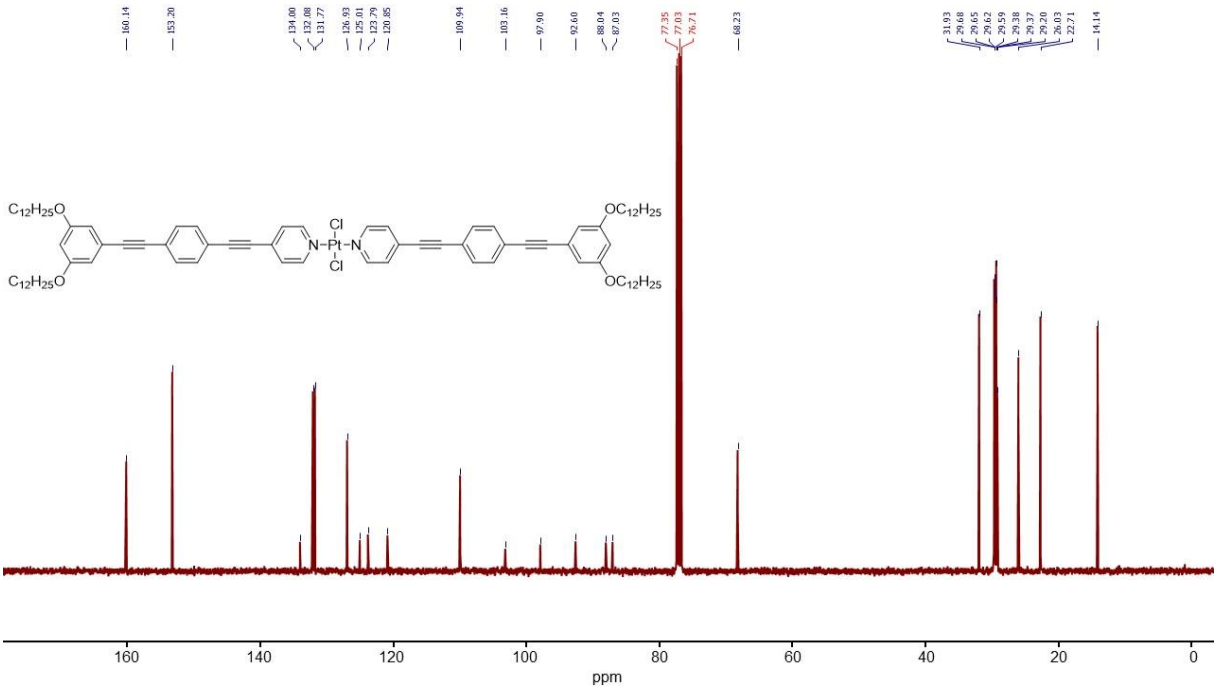

Figure S12: ^{13}C NMR spectrum of **2** (100.6 MHz, $CDCl_3$, 298 K).

4. Supplementary Figures

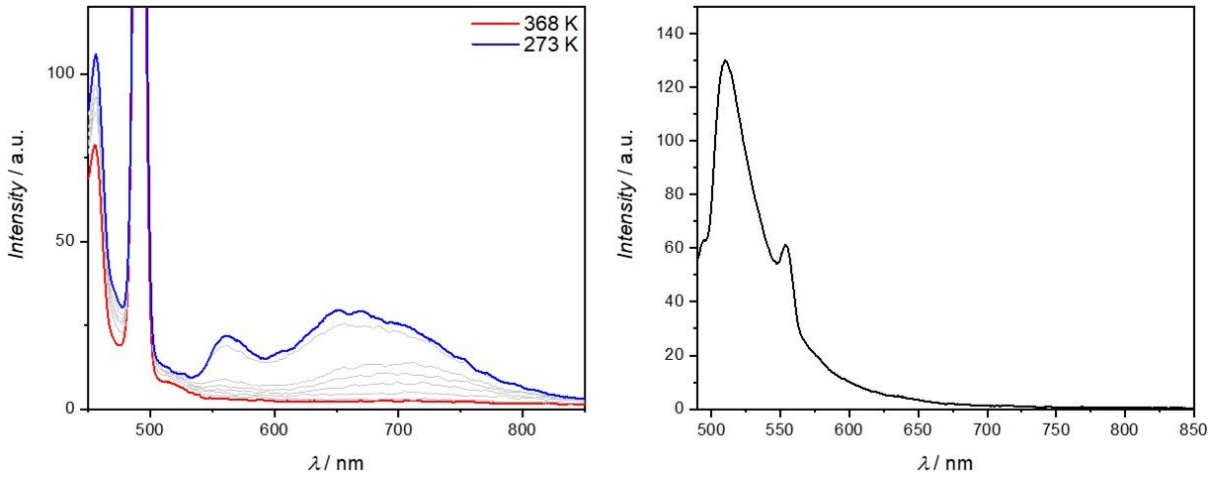

Figure S13: VT-Fluorescence spectra of **1** (c = 3 x 10^{-6} M, $\lambda_{exc.}$ = 430 nm) between 368 K and 273 K in MCH and emission spectrum of **1** (c = 1 x 10^{-5} M, $\lambda_{exc.}$ = 475 nm) at 298 K in chloroform.

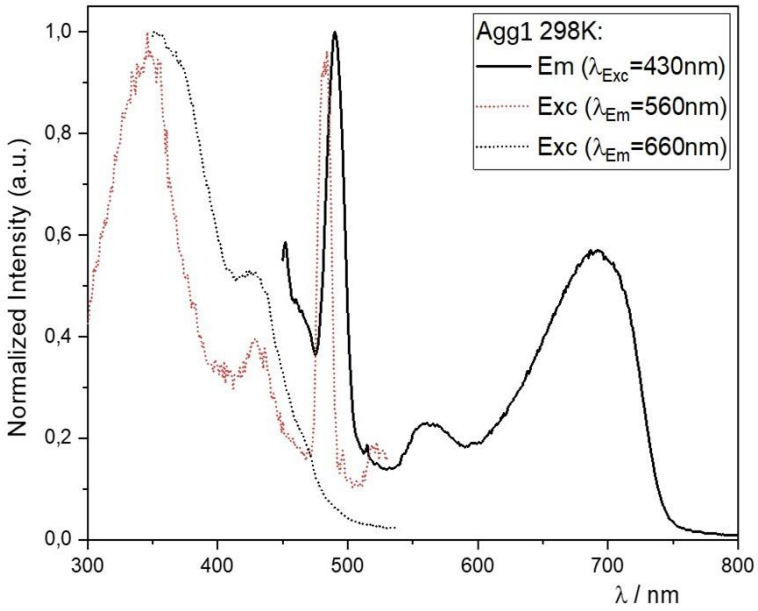

Figure S14: Excitation (dotted line) and emission spectra (solid line) of **Agg1** (λ_{exc} = 430 nm; λ_{em} = 560 nm (red); λ_{em} = 660 nm (black)) at 298 K in MCH. Normalized to the highest intensity. Note that the unusual peak form (steep decline above 720 nm) is caused by limitations from the detector.

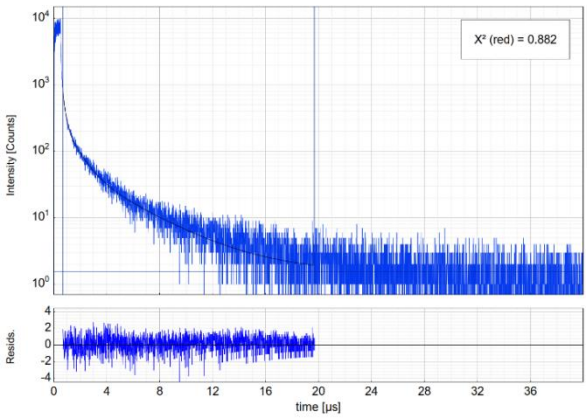

Parameter	Value	Conf. Lower	Conf. Upper	Conf. Estimation
A_1 [Cnts]	59.02	-3.52	+3.52	Fitting
τ_1 [µs]	3.785	-0.167	+0.167	Fitting
A_2 [Cnts]	217.3	-14.3	+14.3	Fitting
τ_2 [µs]	0.9053	-0.0529	+0.0529	Fitting
A_3 [Cnts]	466.2	-51.0	+51.0	Fitting
τ_3 [µs]	0.1659	-0.0204	+0.0204	Fitting
Bkgr. Dec [Cnts]	1.544	-0.400	+0.400	Fitting

Average Lifetime:

$\tau_{Av.1}$=2.084 µs (intensity weighted)

$\tau_{Av.2}$=0.670 µs (amplitude weighted)

Figure S15: Left: Time-resolved luminescence decay of **Agg1** in deaerated MCH at 298 K, including the residuals (λ_{exc} = 376.7 nm, λ_{em} = 690 nm). Right: Fitting parameters including pre-exponential factors and confidence limits.

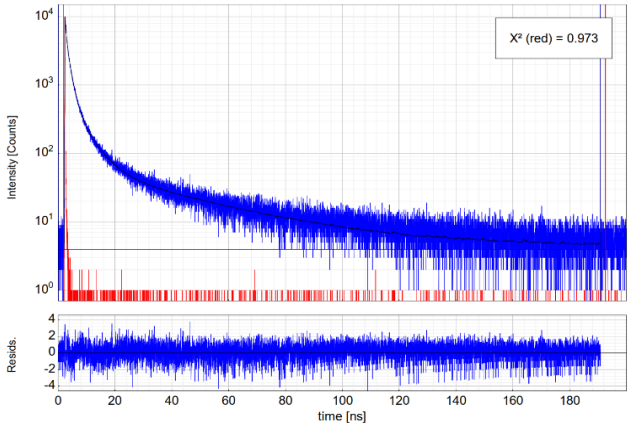

Parameter	Value	Conf. Lower	Conf. Upper	Conf. Estimation
A_1 [Cnts]	64.74	-4.32	+4.32	Fitting
τ_1 [ns]	34.58	-1.72	+1.72	Fitting
A_2 [Cnts]	712.7	-40.6	+40.6	Fitting
τ_2 [ns]	5.210	-0.201	+0.201	Fitting
A_3 [Cnts]	5254	-172	+172	Fitting
τ_3 [ns]	1.3935	-0.0375	+0.0375	Fitting
A_4 [Cnts]	7244	-559	+559	Fitting
τ_4 [ns]	0.3191	-0.0263	+0.0263	Fitting
Bkgr. Dec [Cnts]	3.924	-0.524	+0.524	Fitting
Bkgr. IRF [Cnts]	-0.0334	-0.0471	+0.0471	Fitting
Shift IRF [ns]	1.75771	-0.00407	+0.00407	Fitting
A Scat [Cnts]	9020	-4400	+4400	Fitting

Average Lifetime:

$\tau_{Av.1}$=6.91 ns (intensity weighted)

$\tau_{Av.2}$=1.17 ns (amplitude weighted)

Figure S16: Left: Time-resolved luminescence decay of **Agg1** (blue) and the IRF (red) in deaerated MCH at 298 K, including the residuals (λ_{exc} = 376.7 nm, λ_{em} = 560 nm). Right: Fitting parameters including pre-exponential factors and confidence limits.

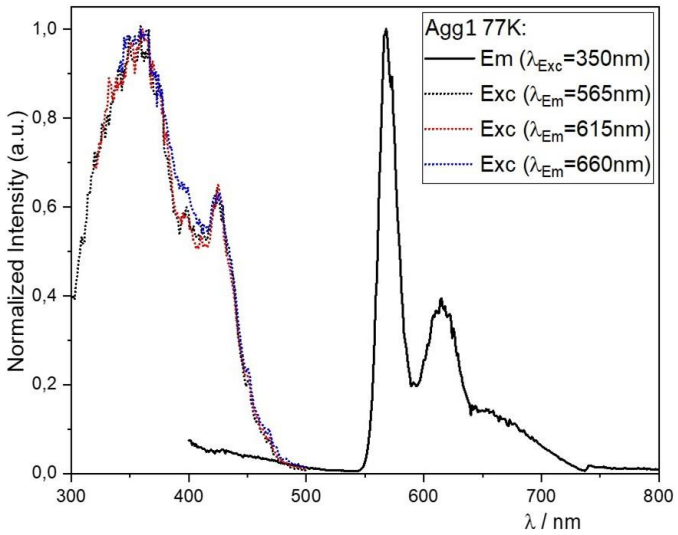

Figure S17: Excitation (dotted line) and emission spectra (solid line) of **Agg1** (λ_{exc} = 350 nm; λ_{em} = 565 nm (black); λ_{exc} = 615 nm (red); λ_{em} = 660 nm (blue)) at 298 K in MCH. Normalized to the highest intensity.

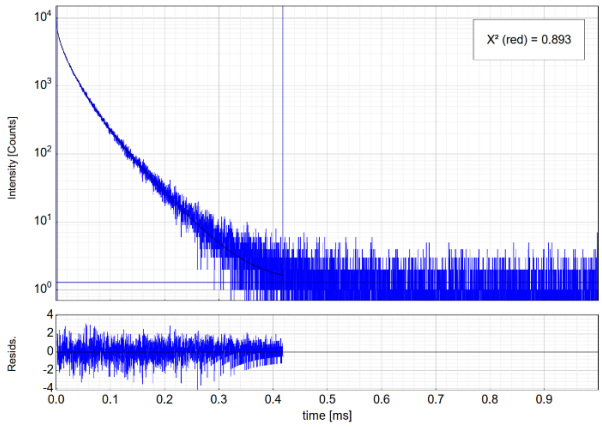

Parameter	Value	Conf. Lower	Conf. Upper	Conf. Estimation
A_1 [Cnts]	1262.1	-21.1	+21.1	Fitting
τ_1 [ms]	0.050936	-0.000500	+0.000500	Fitting
A_2 [Cnts]	3347.7	-51.0	+51.0	Fitting
τ_2 [ms]	0.022003	-0.000293	+0.000293	Fitting
A_3 [Cnts]	2039	-133	+133	Fitting
τ_3 [ms]	0.005497	-0.000431	+0.000431	Fitting
Bkgr. Dec [Cnts]	1.287	-0.479	+0.479	Fitting

Average Lifetime:

$\tau_{Av.1}$=0.033233 ms (intensity weighted)

$\tau_{Av.2}$=0.022433 ms (amplitude weighted)

Figure S18: Left: Time-resolved luminescence decay of **Agg1** in glassy MCH at 77 K, including the residuals (λ_{exc} = 376.7 nm, λ_{em} = 565 nm). Right: Fitting parameters including pre-exponential factors and confidence limits.

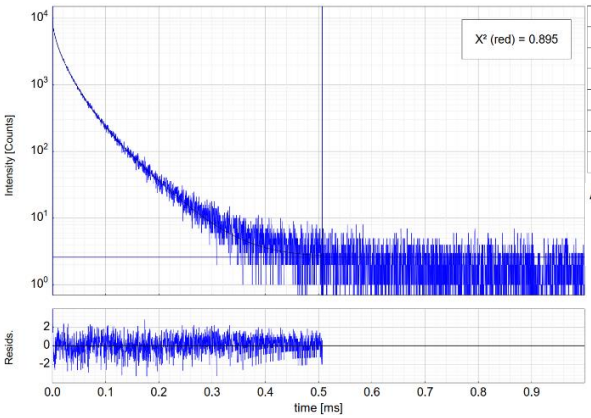

Parameter	Value	Conf. Lower	Conf. Upper	Conf. Estimation
A_1 [Cnts]	1100.1	-20.6	+20.6	Fitting
τ_1 [ms]	0.057035	-0.000630	+0.000630	Fitting
A_2 [Cnts]	3832.6	-59.0	+59.0	Fitting
τ_2 [ms]	0.021329	-0.000288	+0.000288	Fitting
A_3 [Cnts]	2695	-165	+165	Fitting
τ_3 [ms]	0.004807	-0.000358	+0.000358	Fitting
Bkgr. Dec [Cnts]	2.595	-0.494	+0.494	Fitting

Average Lifetime:

$\tau_{Av.1}$=0.034200 ms (intensity weighted)

$\tau_{Av.2}$=0.020642 ms (amplitude weighted)

Figure S19: Left: Time-resolved luminescence decay of **Agg1** in glassy MCH at 77 K, including the residuals (λ_{exc} = 376.7 nm, λ_{em} = 615 nm). Right: Fitting parameters including pre-exponential factors and confidence limits.

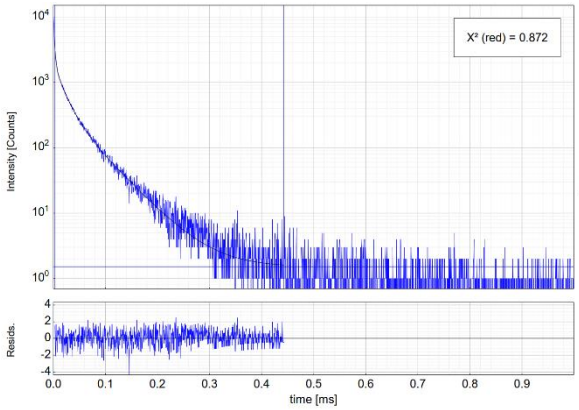

Parameter	Value	Conf. Lower	Conf. Upper	Conf. Estimation
A_1 [Cnts]	455.7	-11.7	+11.7	Fitting
τ_1 [ms]	0.052204	-0.000863	+0.000863	Fitting
A_2 [Cnts]	1231.9	-36.5	+36.5	Fitting
τ_2 [ms]	0.016623	-0.000459	+0.000459	Fitting
A_3 [Cnts]	1404	-130	+130	Fitting
τ_3 [ms]	0.002322	-0.000281	+0.000281	Fitting
Bkgr. Dec [Cnts]	1.516	-0.391	+0.391	Fitting

Average Lifetime:

$\tau_{Av.1}$=0.033452 ms (intensity weighted)

$\tau_{Av.2}$=0.015373 ms (amplitude weighted)

Figure S20: Left: Time-resolved luminescence decay of **Agg1** in glassy MCH at 77 K, including the residuals (λ_{exc} = 376.7 nm, λ_{em} = 660 nm). Right: Fitting parameters including pre-exponential factors and confidence limits.

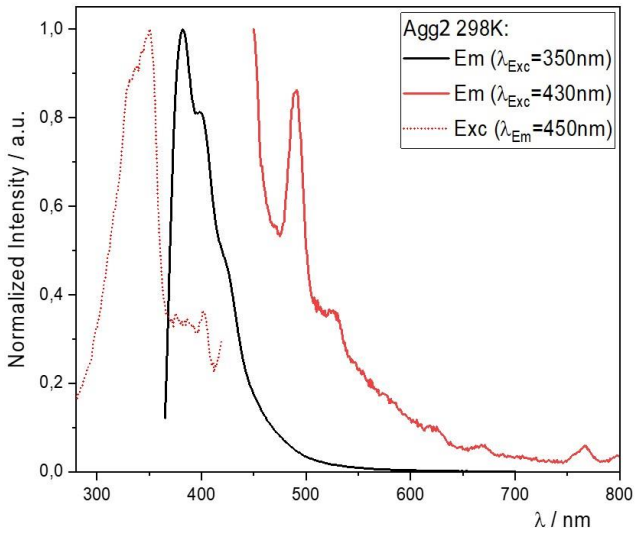

Figure S21: Excitation (dotted line) and emission spectra (solid line) of **Agg2** (λ_{exc} = 350 nm (black); λ_{exc} = 430 nm (red); λ_{em} = 450 nm) at 298 K in MCH. Normalized to the highest intensity.

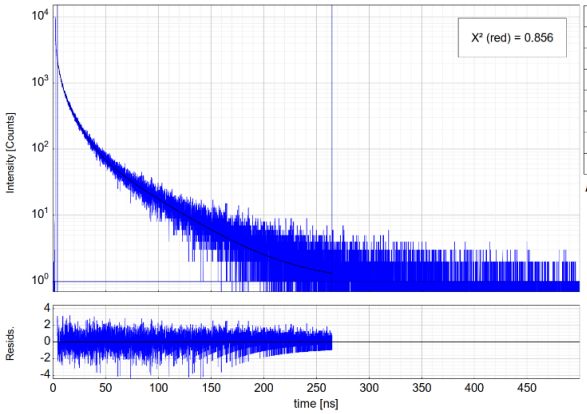

Parameter	Value	Conf. Lower	Conf. Upper	Conf. Estimation
A_1 [Cnts]	157.14	-6.36	+6.36	Fitting
τ_1 [ns]	42.42	-1.10	+1.10	Fitting
A_2 [Cnts]	861.1	-27.6	+27.6	Fitting
τ_2 [ns]	11.209	-0.300	+0.300	Fitting
A_3 [Cnts]	1158.6	-78.3	+78.3	Fitting
τ_3 [ns]	2.875	-0.215	+0.215	Fitting
Bkgr. Dec [Cnts]	0.993	-0.390	+0.390	Fitting

Average Lifetime:

$\tau_{Av.1}$=20.39 ns (intensity weighted)

$\tau_{Av.2}$=9.03 ns (amplitude weighted)

Figure S22: Left: Time-resolved luminescence decay of **Agg2** in deaerated MCH at 298 K, including the residuals (λ_{exc} = 376.7 nm, λ_{em} = 450 nm). Right: Fitting parameters including pre-exponential factors and confidence limits.

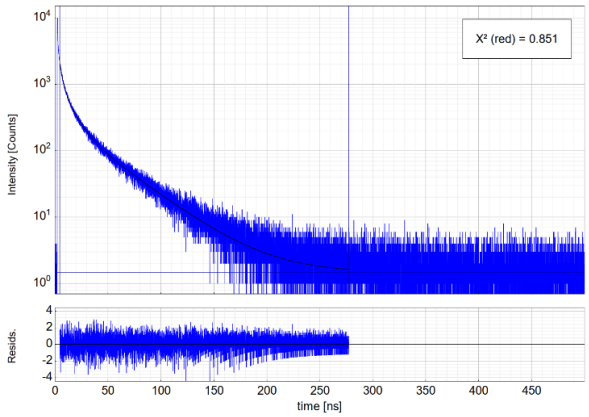

Parameter	Value	Conf. Lower	Conf. Upper	Conf. Estimation
A_1 [Cnts]	751.3	-31.6	+31.6	Fitting
τ_1 [ns]	9.643	-0.367	+0.367	Fitting
A_2 [Cnts]	274.42	-8.30	+8.30	Fitting
τ_2 [ns]	36.786	-0.747	+0.747	Fitting
A_3 [Cnts]	1050.3	-82.3	+82.3	Fitting
τ_3 [ns]	2.602	-0.230	+0.230	Fitting
Bkgr. Dec [Cnts]	1.474	-0.395	+0.395	Fitting

Average Lifetime:

$\tau_{Av.1}$=22.335 ns (intensity weighted)

$\tau_{Av.2}$=9.668 ns (amplitude weighted)

Figure S23: Left: Time-resolved luminescence decay of **Agg2** in deaerated MCH at 298 K, including the residuals (λ_{exc} = 376.7 nm, λ_{em} = 550 nm). Right: Fitting parameters including pre-exponential factors and confidence limits.

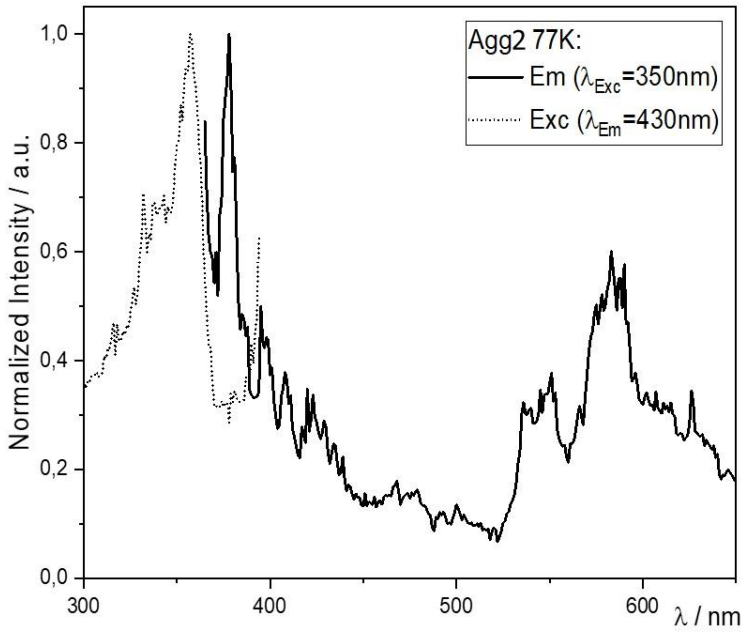

Figure S24: Excitation (dotted line) and emission spectra (solid line) of **Agg2** (λ_{exc} = 350 nm; λ_{exc} = 430 nm) at 77 K in MCH. Normalized to the highest intensity.

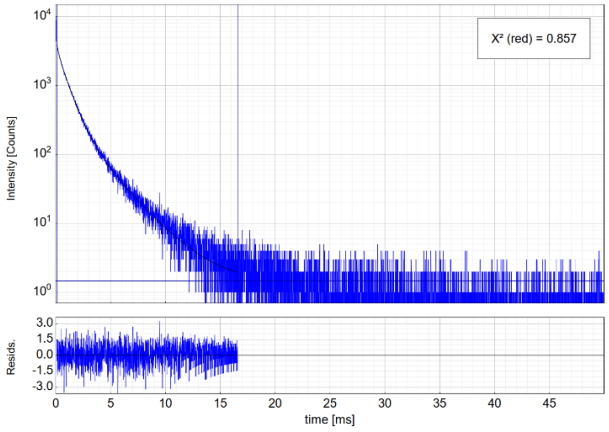

Parameter	Value	Conf. Lower	Conf. Upper	Conf. Estimation
A_1 [Cnts]	391.3	-11.5	+11.5	Fitting
τ_1 [ms]	2.4773	-0.0416	+0.0416	Fitting
A_2 [Cnts]	2793.8	-40.2	+40.2	Fitting
τ_2 [ms]	0.8358	-0.0103	+0.0103	Fitting
A_3 [Cnts]	789	-107	+107	Fitting
τ_3 [ms]	0.1989	-0.0332	+0.0332	Fitting
Bkgr. Dec [Cnts]	1.466	-0.470	+0.470	Fitting

Average Lifetime:

$\tau_{Av.1}$=1.2666 ms (intensity weighted)

$\tau_{Av.2}$=0.8710 ms (amplitude weighted)

Figure S25: Left: Time-resolved luminescence decay of **Agg2** in glassy MCH at 77 K, including the residuals (λ_{exc} = 376.7 nm, λ_{em} = 550 nm). Right: Fitting parameters including pre-exponential factors and confidence limits.

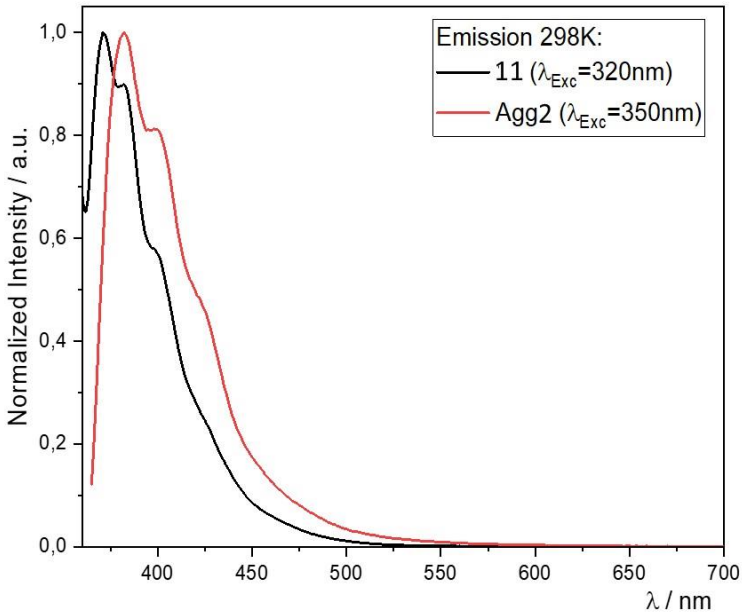

Figure S26: Emission spectra of reference ligand **11** (λ_{exc} = 320 nm (black)) and **Agg2** (λ_{exc} = 430 nm (red)) at 298 K in MCH. Normalized to the highest intensity.

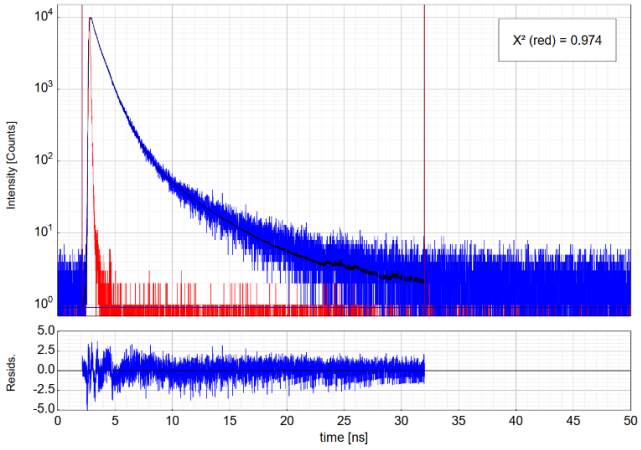

Parameter	Value	Conf. Lower	Conf. Upper	Conf. Estimation
A_1 [Cnts]	40.71	-1.85	+1.85	Fitting
τ_1 [ns]	3.8229	-0.0913	+0.0913	Fitting
A_2 [Cnts]	1256.4	-13.1	+13.1	Fitting
τ_2 [ns]	0.95833	-0.00754	+0.00754	Fitting
A_3 [Cnts]	498.2	-31.6	+31.6	Fitting
τ_3 [ns]	0.3222	-0.0219	+0.0219	Fitting
Bkgr. Dec [Cnts]	0.927	-0.453	+0.453	Fitting
Bkgr. IRF [Cnts]	-0.0503	-0.0598	+0.0598	Fitting
Shift IRF [ns]	0.00159	-0.00171	+0.00171	Fitting
A Scat [Cnts]	130380	-7200	+7200	Fitting
Period Rep [ns]	0.010083	-0.000696	+0.000696	Fitting

Average Lifetime:

$\tau_{Av.1}$=1.1844 ns (intensity weighted)

$\tau_{Av.2}$=0.8468 ns (amplitude weighted)

Figure S27: Left: Time-resolved luminescence decay of **11** (blue) and the Instrument Response Function (IRF, red) in deaerated MCH at 298 K, including the residuals (λ_{exc} = 376.7 nm, λ_{em} = 450 nm). Right: Fitting parameters including pre-exponential factors and confidence limits.

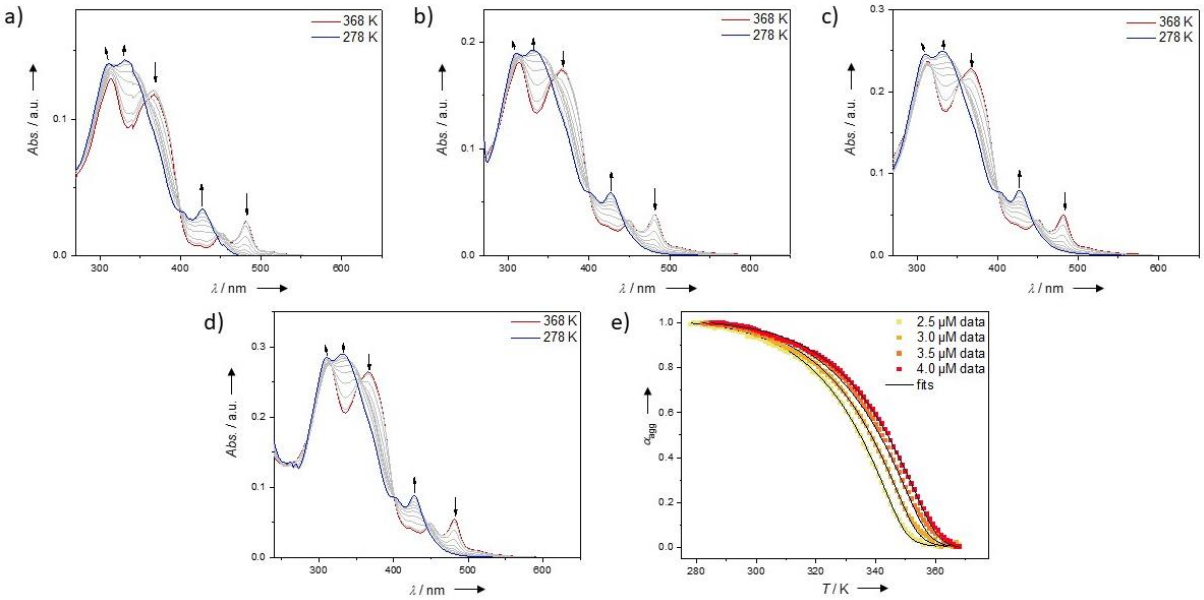

Figure S28: Variable temperature (VT)-UV-Vis spectra of **1** at c = 2.5 x 10^{-6} M (a); 3.0 x 10^{-6} M (b); 3.5 x 10^{-6} M (c); and 4 x 10^{-6} M (d) in MCH between 368 K and 278 K with the degree of aggregation α_{agg} (calculated from the depletion of the absorbance at λ = 475 nm) plotted *vs.* temperature T and fits obtained from nucleation-elongation model (e).[7]

Table S1: Thermodynamic parameters ΔH_e; ΔH_n; ΔS; T_e; K_e; K_n and σ derived from VT-UV-Vis experiments of **1** (MCH, λ= 475 nm) on the basis of the nucleation-elongation model using a global fitting approach.[7]

Concentration / 10^{-6} M	ΔH_e (SD) / kJ mol^{-1}	ΔH_n (SD) / kJ mol^{-1}	ΔS (SD) / kJ mol^{-1}	T_e (SD) / K	K_e / 10^5 M^{-1}	K_n / 10^2 M^{-1}	σ / 10^{-3}
2.5	-48.88 (0.25)	-17.27 (0.19)	-0.0336 (0.0008)	347.12 (0.07)	4.00	10.07	2.52
3.0	-48.88 (0.25)	-17.27 (0.19)	-0.0336 (0.0008)	351.58 (0.09)	3.23	8.76	2.71
3.7	-48.88 (0.25)	-17.27 (0.19)	-0.0336 (0.0008)	355.34 (0.11)	2.70	7.81	2.89
4.0	-48.88 (0.25)	-17.27 (0.19)	-0.0336 (0.0008)	357.02 (0.12)	2.50	7.43	2.97

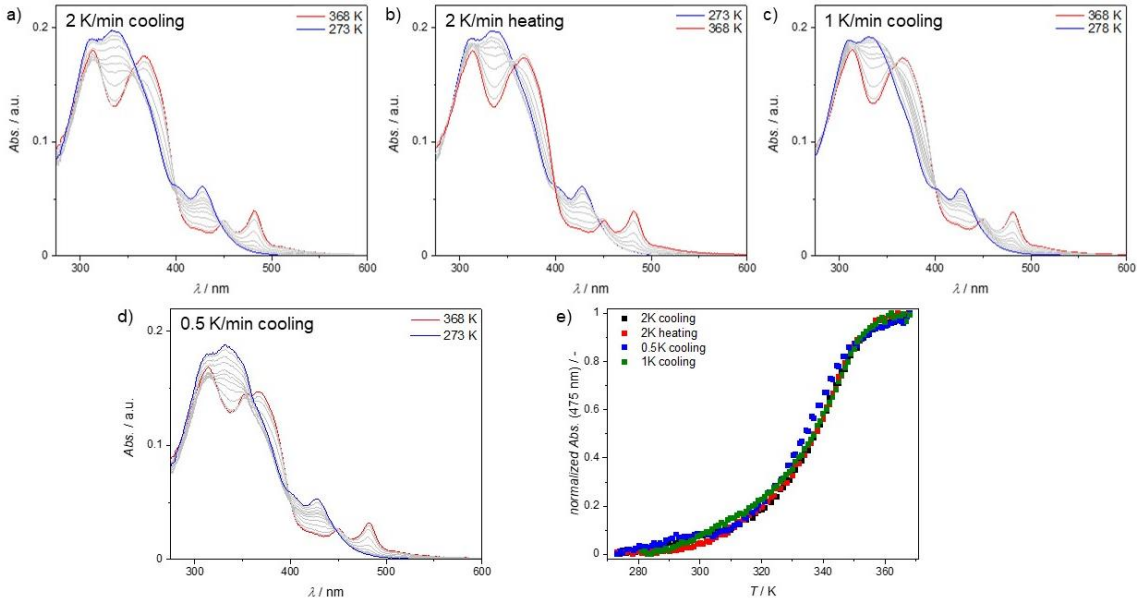

Figure S29: Cooling rate-dependent VT-UV-Vis spectra of **1** at c = 3.0 x 10^{-6} M in MCH between 368 K and 273 K (a-d). Normalized absorbance (λ_{abs} = 475 nm) plotted against the temperature (T) for different cooling rates.

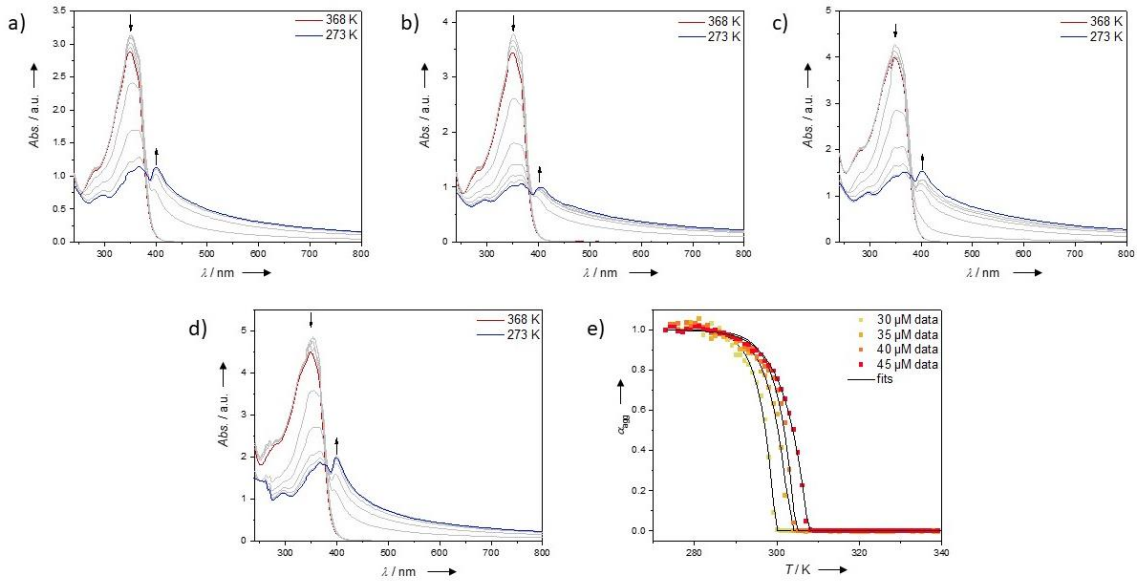

Figure S30: Variable temperature (VT)-UV-Vis spectra of **2** at c = 30 x 10^{-6} M (a); 35 x 10^{-6} M (b); 40 x 10^{-6} M (c); and 45 x 10^{-6} M (d) in MCH between 368 K and 273 K while stirring with the degree of aggregation α_{agg} (calculated from the increase of the absorbance at λ = 450 nm) plotted vs. temperature T and fits obtained from nucleation-elongation model (e).[7]

Table S2: Thermodynamic parameters ΔH_e; ΔH_n; ΔS; T_e; K_e; K_n and σ derived from VT-UV-Vis experiments of **2** (MCH, λ = 450 nm) on the basis of the nucleation-elongation model using a global fitting approach.[7]

Concentration / 10^{-6} M	ΔH_e (SD) / kJ mol^{-1}	ΔH_n (SD) / kJ mol^{-1}	ΔS (SD) / kJ mol^{-1}	T_e (SD) / K	K_e / 10^4 M^{-1}	K_n / M^{-1}	σ / 10^{-4}
30	-189.09 (1.26)	-22.49 (1.98)	-0.535 (0.004)	299.93 (0.03)	10.00	12.09	1.21
35	-189.09 (1.26)	-22.49 (1.98)	-0.535 (0.004)	302.69 (0.04)	5.00	6.56	1.31
40	-189.09 (1.26)	-22.49 (1.98)	-0.535 (0.004)	304.34 (0.04)	3.33	4.59	1.38
45	-189.09 (1.26)	-22.49 (1.98)	-0.535 (0.004)	307.19 (0.06)	1.67	2.49	1.50

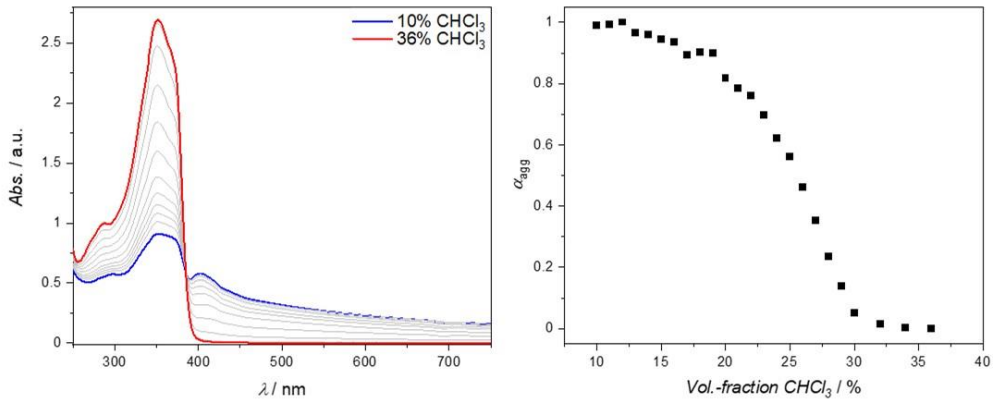

Figure S31: Solvent-dependent denaturation studies of **Agg2** at c = 3 x 10^{-5} M and T = 298 K between 10 and 36% chloroform in MCH.

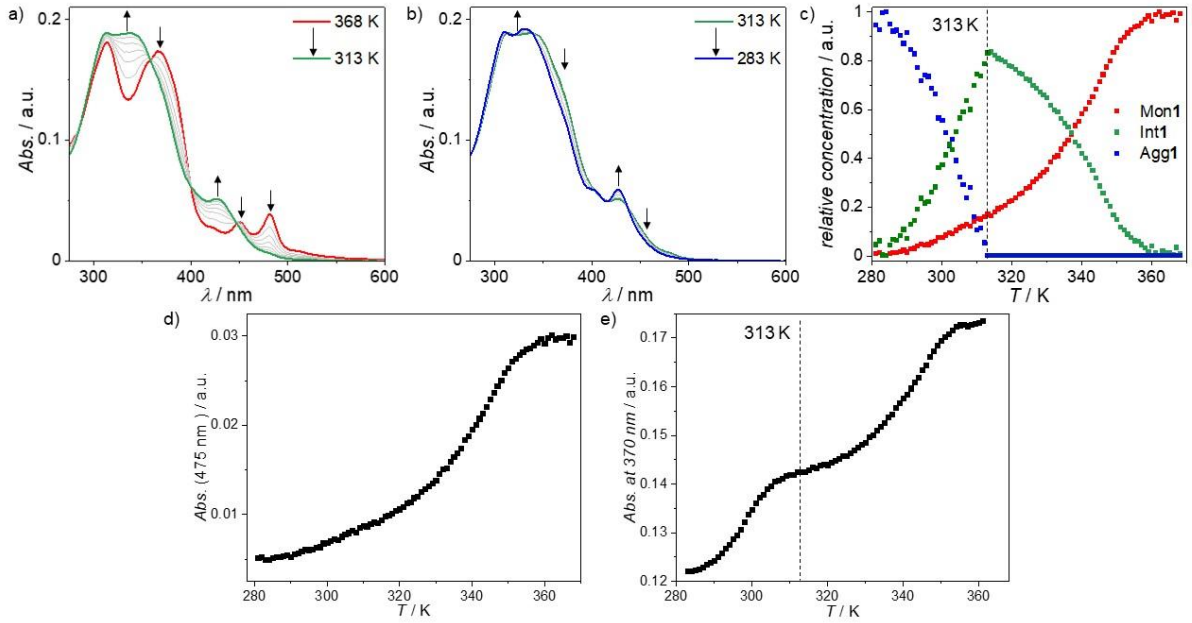

Figure S32: VT-UV/Vis spectra of **1** between 363 K and 313 K (a) and 313 K and 283 K (b) at 3 x 10^{-6} M; cooling rate: 1 K/min. c) Relative concentration of the different species involved in the aggregation process plotted *vs. T*. estimated based on the spectral changes at λ = 475 (d) nm and λ = 370 nm (e) during VT-UV/Vis studies

In order to estimate the concentrations of all active species during the temperature dependent aggregation of **1** mainly two wavelengths have been used. After identifying the characteristic absorption band of the monomer species **Mon1** (475 nm, d) the concentration can be directly calculated for the entire cooling process by normalizing the spectral changes (c, red dots). Following this simple determination of the monomer concentration, we analyzed a wavelength characteristic for the transition between both species (370 nm, e). Interestingly, the transition point (313 K) matches the switching between both temperature regimes in which distinct isosbestic points are appreciable (a, b). Based on this observation, we divided the relative concentration estimation into two regimes (368 – 314 and 313 – 283 K respectively). For the first temperature regime, we approximated the concentration of **Agg1** to 0, while for the concentration of the monomer is known based on the spectral changes at 475 nm and the total concentration must be 1 at all times, which gives the concentration of **Int1**, leading to the following equations for the first temperature regime:

$$c_{Mon1}(T) = \frac{Abs._{475\,nm}(T) - Abs._{475nm}(283\ \mathrm{K})}{Abs._{475nm}(368\ \mathrm{K}) - Abs._{475nm}(283\ \mathrm{K})} \quad (1)$$

$$c_{Int1}(T) = 1 - c_{Mon1}(T) \quad (2)$$

For the second temperature regime, two simple approximations have been made for the system:
1) The remaining monomer consumption is transformed directly into **Agg1**.
2) The transformation from **Int1** to **Agg1** starts immediately at 313 K.
These approximations allow us to estimate the concentration of **Agg1** from the normalized decrease of the concentration of **Mon1** in the second temperature regime. Additionally, the concentration of **Int1** has been calculated based on the fundamental requirement that the total concentration of all species must remain 1 at all times, while equation (1) applies for both temperature regimes leading to the following equations for the second temperature regime:

$$c_{Agg1}(T) = \frac{c_{Mon1}(T) - c_{Mon1}(313\ \mathrm{K})}{-c_{Mon1}(313\ \mathrm{K})} \quad (3)$$

$$c_{Int1}(T) = 1 - \left(c_{Mon1}(T) + c_{Agg1}(T)\right) \quad (4)$$

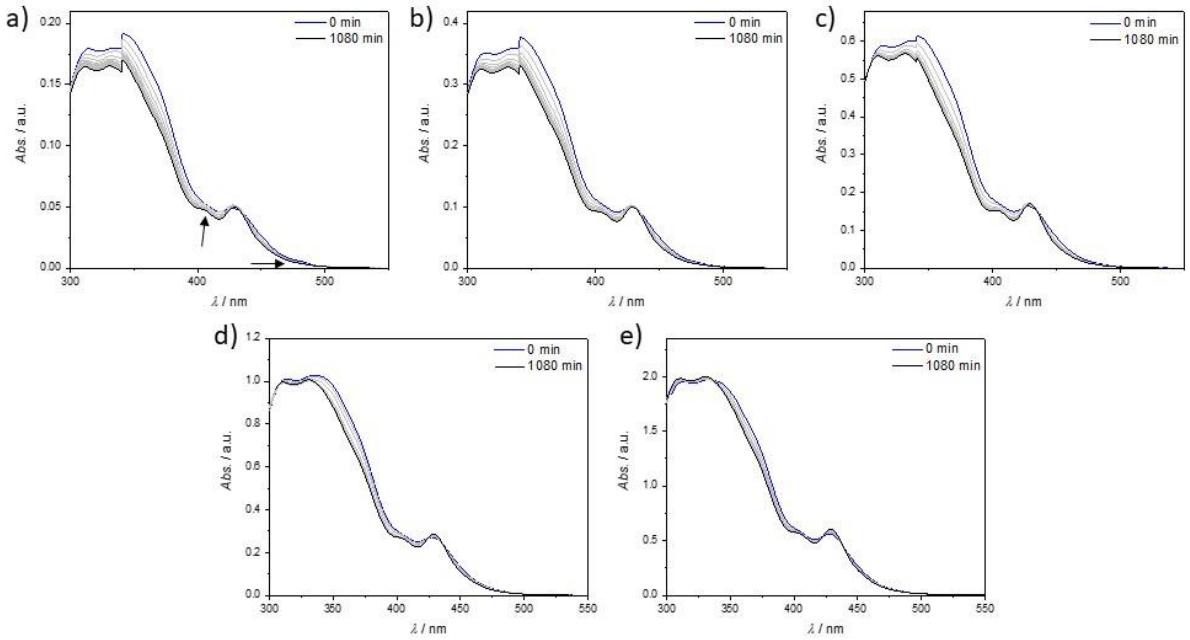

Figure S33: Time-dependent UV/Vis spectra of **1** at 298 K after rapidly cooling from 368 K in MCH at c = 2.5 x 10^{-6} M (a), c = 5 x 10^{-6} M (b), c = 7.5 x 10^{-6} M (c), c = 10 x 10^{-6} M (d), c = 20 x 10^{-6} M (e) showing the transformation from the kinetic intermediate species **Int1** to the thermodynamic aggregate **Agg1**. Arrows indicate the spectral features indicating the incomplete transformation during the measurement at c = 2.5 x 10^{-6} M (a).

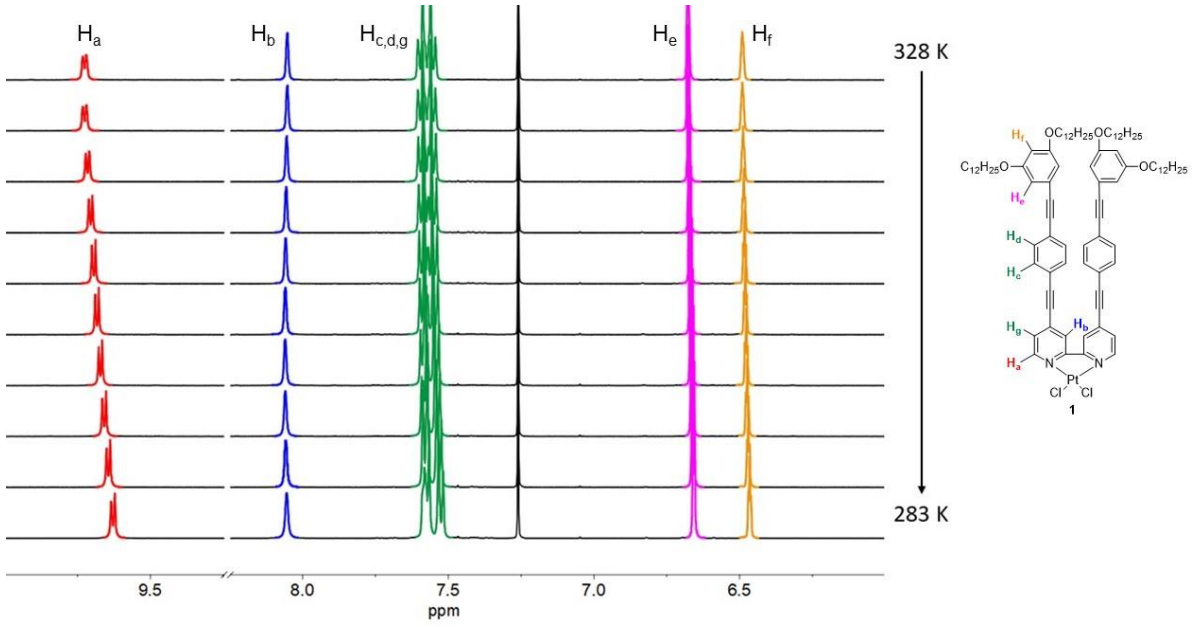

Figure S34: VT-^{1}H NMR spectra of **1** between 328 K and 283 K in steps of 5 K in $CDCl_3$ at c = 1 x 10^{-3} M.

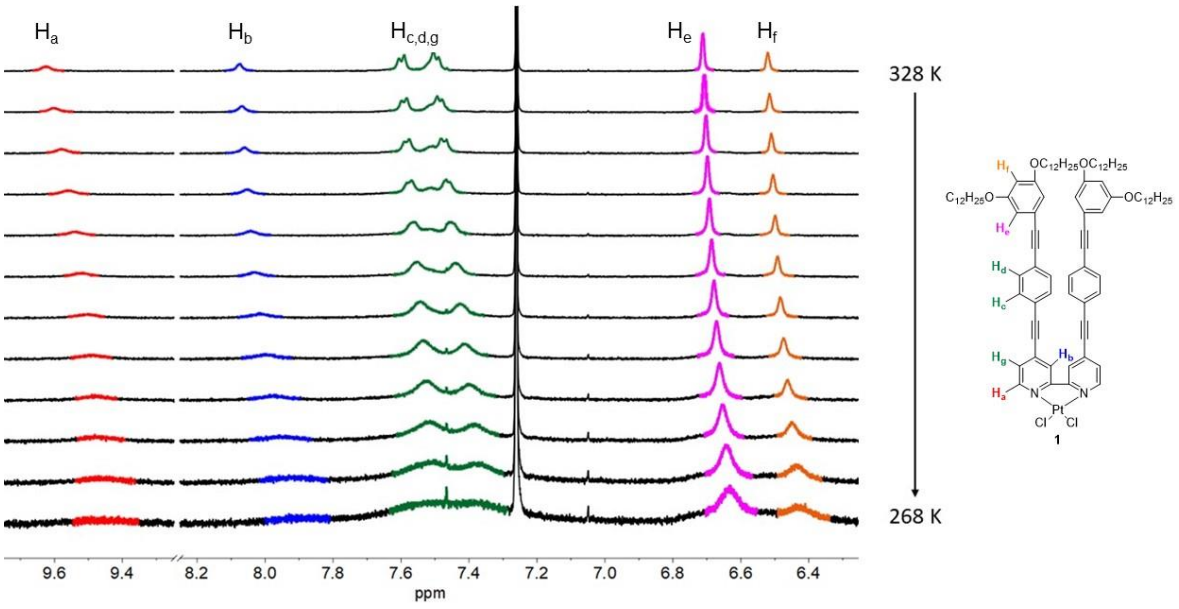

Figure S35: VT-^{1}H NMR spectra of **1** between 328 K and 268 K in steps of 5 K in $CDCl_3$/MCH-d_{14} (4:6) at c = 1 x 10^{-3} M.

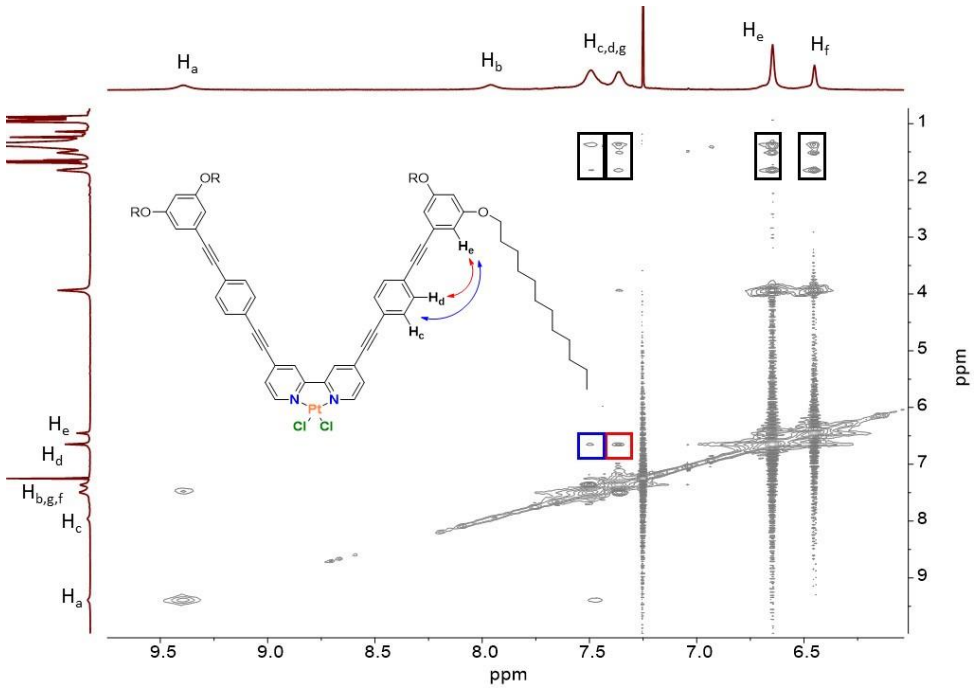

Figure S36: 2D-ROESY-NMR spectrum of **1** in a mixture of $CDCl_3$/MCH-d_{14} (4:6) at c = 7.5 x 10^{-3} M and T = 298 K. Colored boxes show the most significant intermolecular interactions. Inset: schematic representation of the possible intra-/ intermolecular close contacts involving aromatic protons indicated with colored arrows (Only one molecule is shown for reasons of clarity).

2D ROESY studies of **1** (Fig. S34) reveal only a few correlations between different aromatic protons despite their obvious involvement in aromatic interactions. In particular, only interactions between the outer phenyl ring and the middle ring of the aromatic backbone can be observed (red/blue squares), which can most likely be explained by intramolecular close contacts, or a minor translational offset within the stack. In contrast, the protons from the bipyridine moiety show no intermolecular close contacts, which supports the proposed parallel molecular stacking. Further, the only interactions involving the alkyl chains stem from close contacts with both the peripheral and the middle phenyl ring. These observations indicate the importance of the alkyl chains in stabilizing the stack, which efficiently shield the aromatic moieties from the aliphatic environment (MCH).

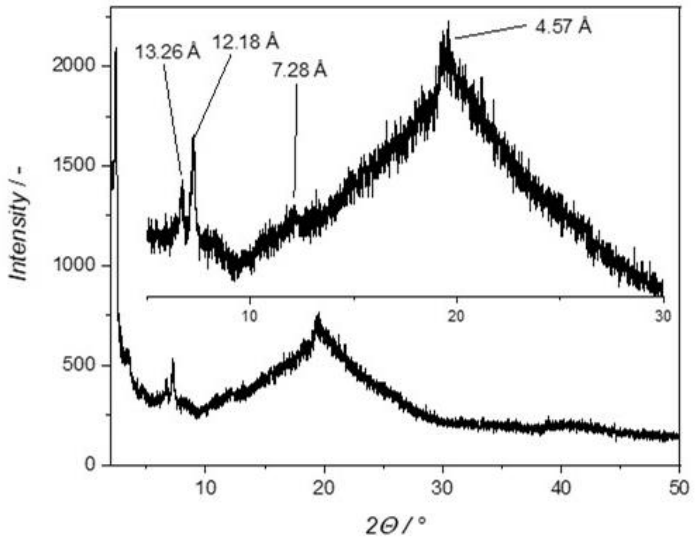

Figure S37: XRD diffraction pattern (λ = 1.5406 Å) of a thin film of **Agg1** obtained from drop-casting a 7.5 x 10^{-3} M solution (chloroform: MCH 4:6) between 2 and 50° with an inset of the region between 5 and 30°.

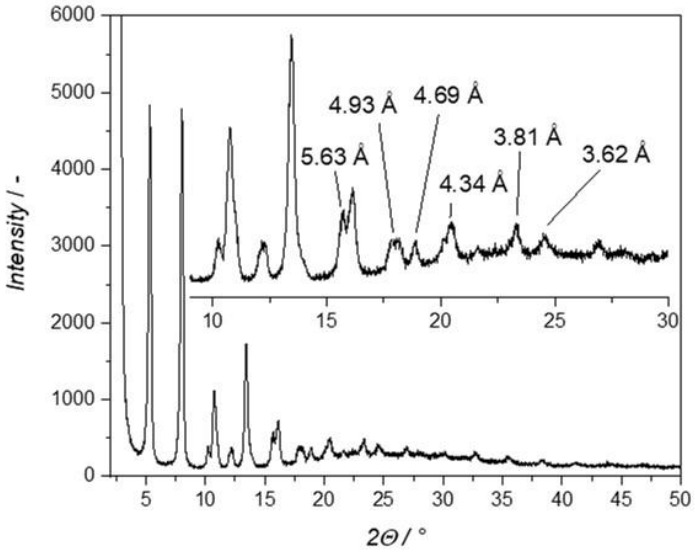

Figure S38: XRD diffraction pattern (λ = 1.5406 Å) of a thin film of **Agg2** obtained from drop-casting a 1 x 10^{-3} M solution (chloroform: MCH 2:8) between 2 and 50° with an inset of the region between 8 and 30°.

XRD analysis for **Agg1** (Fig. S35) shows a very broad featureless reflex between 2Θ = 12° and 30°, which can be rationalized by a potential flexibility of the 1D stack. XRD of **Agg2** (Fig. S36) was recorded using the precipitate obtained from solvent-dependent NMR studies. The molecular structure of **2** is similar to previously reported analogues from our group[8] and, therefore, we hypothesize a similar packing in the aggregated state. Accordingly, we compared the reflexes and the corresponding distances with results obtained from a single crystal X-ray diffractometric analysis of a trimethoxy-appended OPE-based bispyridyldichlorido Pt(II) complex.[8] Hence, we tentatively attribute the reflex corresponding to 3.62 Å to the intermolecular distance between the aromatic moieties. Further, we attribute the reflexes at 2Θ = 20.46 Å and 18.93 Å, corresponding to distances of 4.34 and 4.69 Å, to the intermolecular Pt···Cl and Pt···Pt distance, respectively.[8] In a previously published example, the dihedral angle between the N-Pt-Cl and the C-N-Pt planes was reported to be 49°,[8] leading to smaller intermolecular distances between Pt and the Cl atom of a neighboring molecule compared to the intermolecular Pt···Pt distance. Accordingly, we assign the reflex at 4.69 Å to the intermolecular Pt···Pt distance. Further reflexes corresponding to distances between 5 and 10 Å can be explained by diagonal distances between neighboring stacks in a 3D assembly.

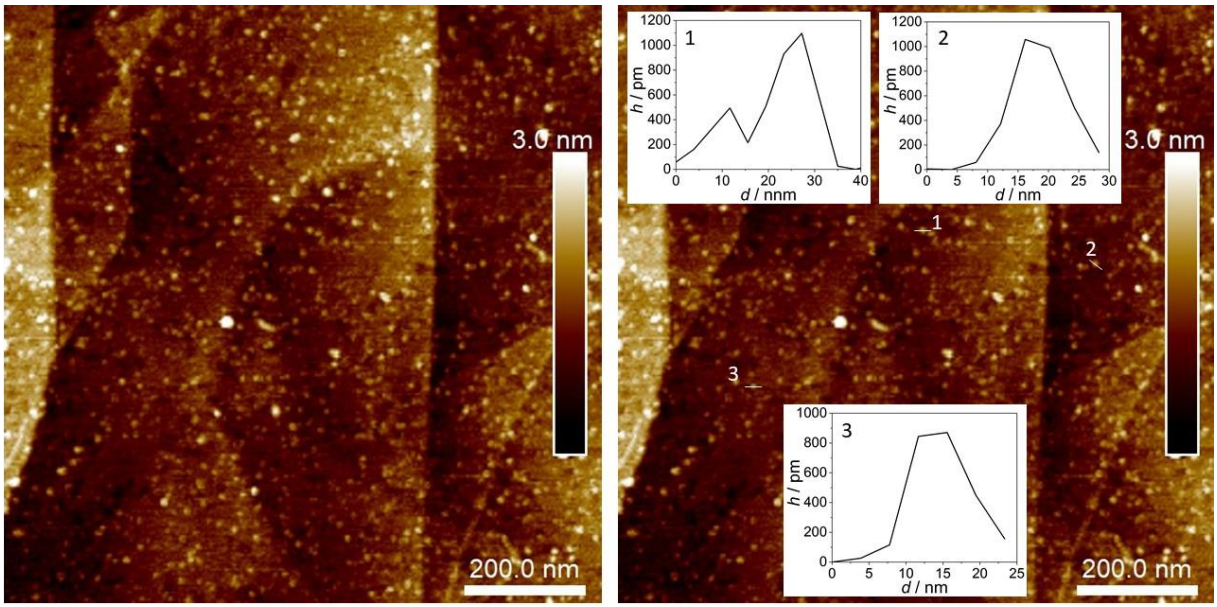

Figure S39: AFM height images of **Int1** at c = 2 x 10^{-5} M after cooling from 368 K to 313 K in MCH (left) with detailed height analysis (right). The samples have been spin-coated onto HOPG using a volume of 20 µL.

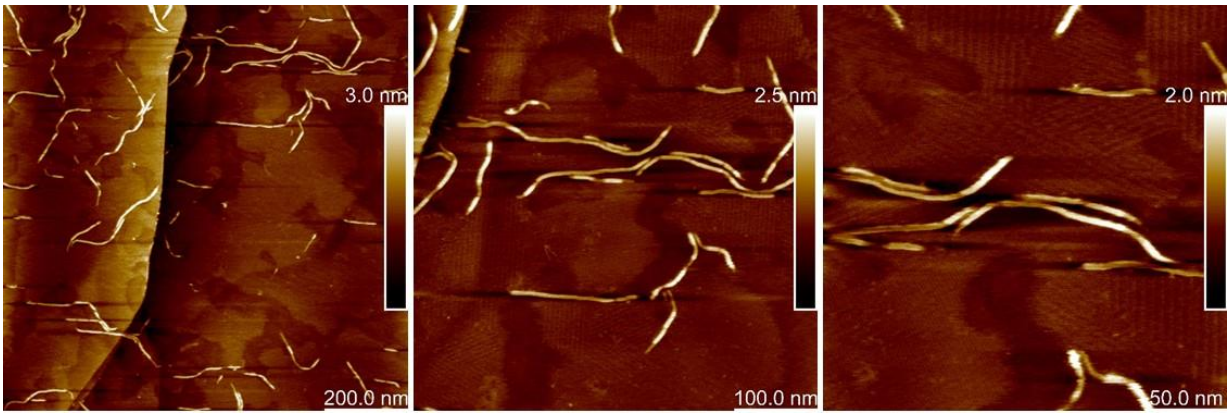

Figure S40: AFM height images of **Agg1** at c = 2 x 10^{-5} M after cooling from 368 K to 273 K in MCH. The samples have been spin-coated onto HOPG using a volume of 20 µL.

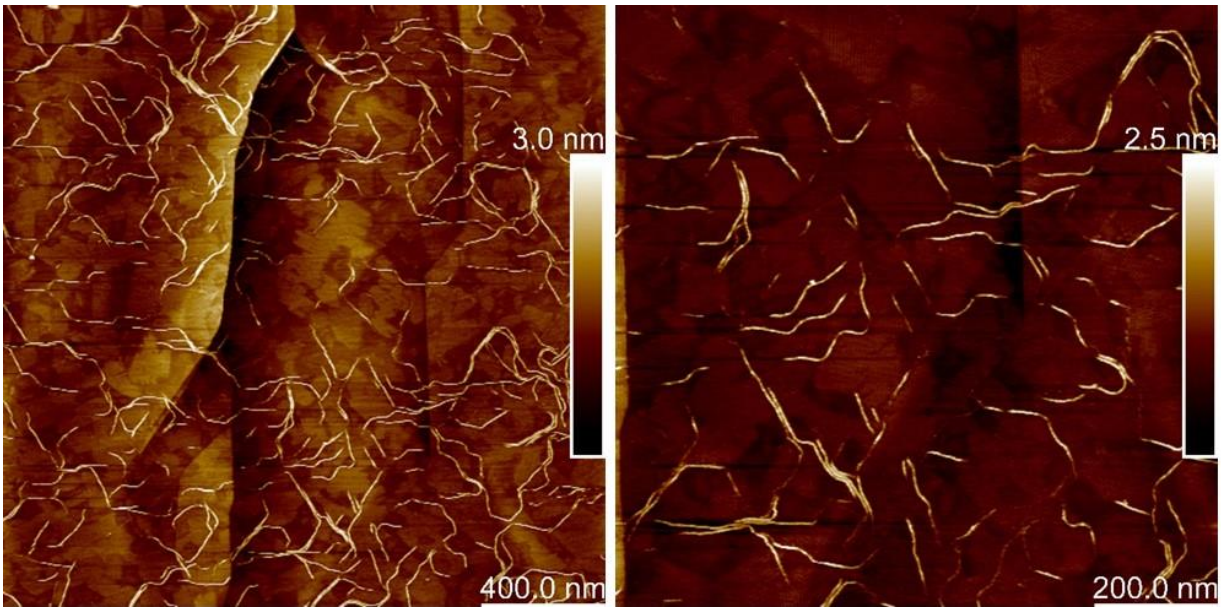

Figure S41: AFM height images of **Agg1** at c = 2 x 10^{-5} M after cooling from 368 K to 273 K in MCH. The samples have been spin-coated using a volume of 20 µL, showing minor bundling on the HOPG surface.

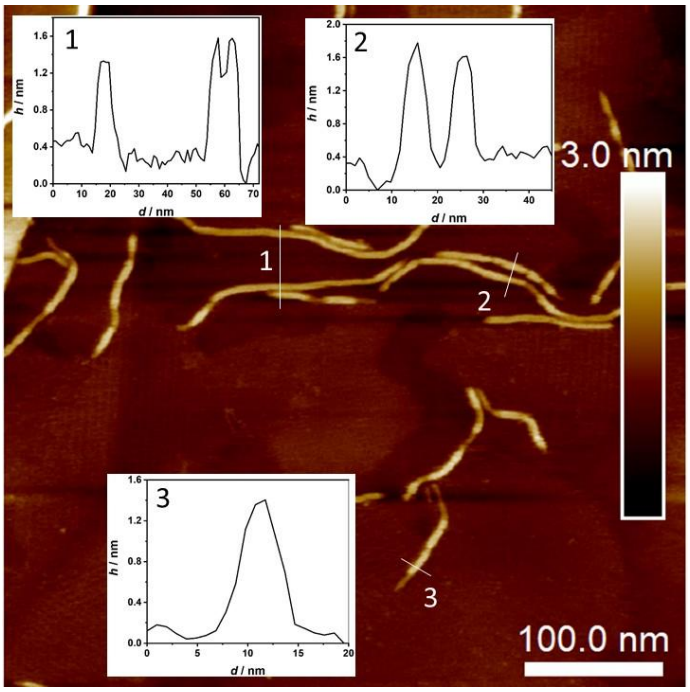

Figure S42: AFM height images of **Agg1** at c = 2 x 10^{-5} M after cooling from 368 K to 273 K in MCH, with the cross-section analysis at various points depicted as insets. The samples have been spin-coated onto HOPG using a volume of 20 µL.

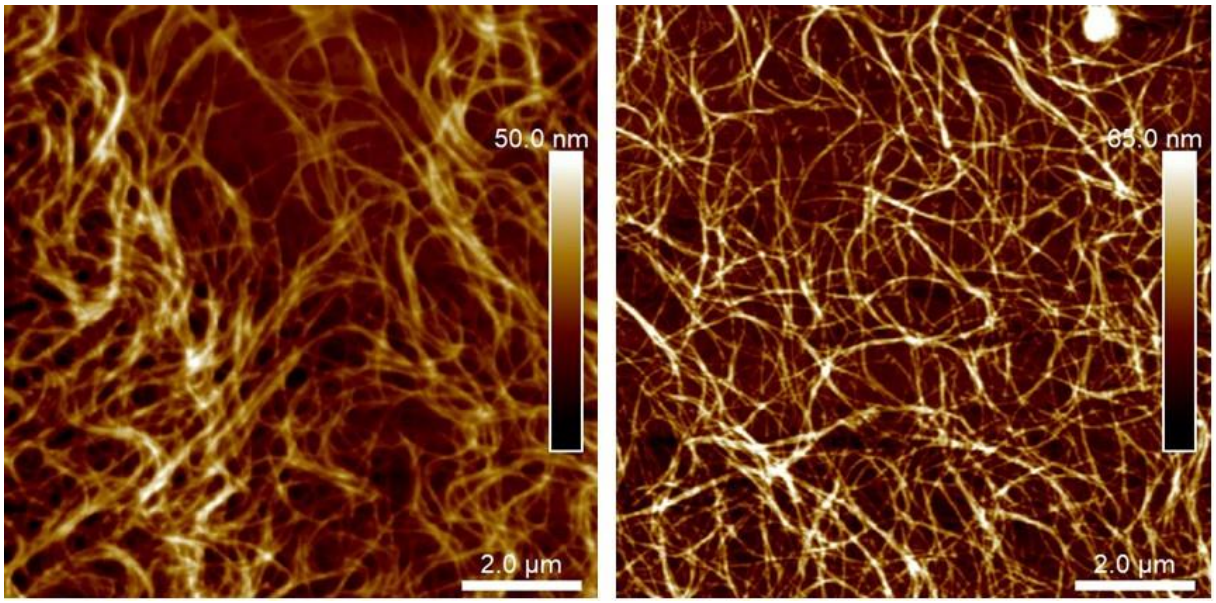

Figure S43: AFM height images of **Agg1** at c = 5 x 10^{-5} M after cooling from 368 K to 298 K in MCH. The samples have been drop-casted using a volume of 10 µL, highlighting the fiber network formation.

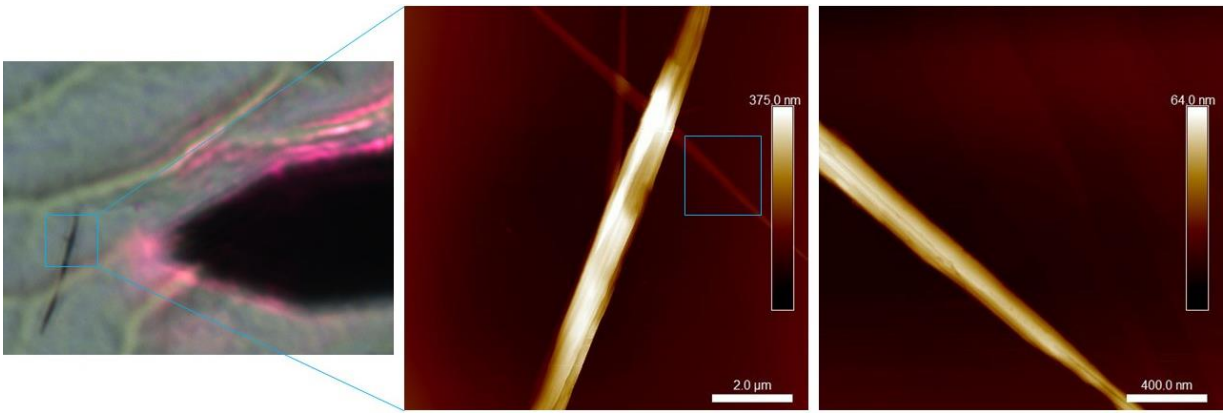

Figure S44: Light microscope (left) and AFM height images without shaking (right) of **Agg2** at c = 2 x 10^{-5} M after cooling from 368 K to 273 K in MCH. The samples have been spin-coated onto HOPG using a volume of 20 µL.

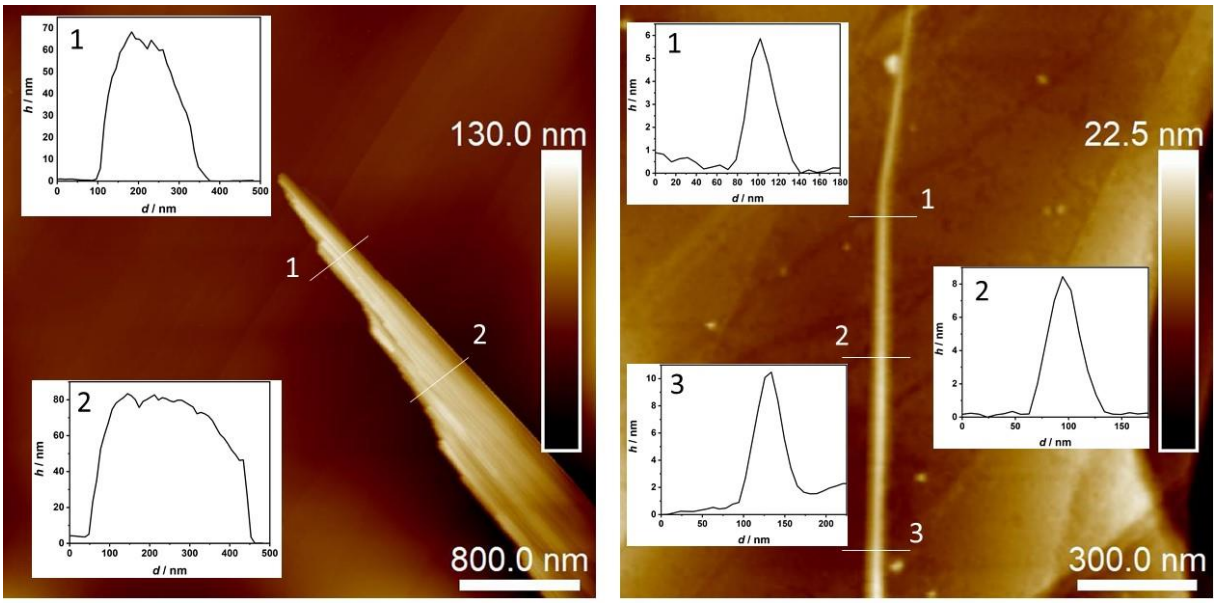

Figure S45: AFM height images of **Agg2** at c = 2 x 10^{-5} M after cooling from 368 K to 273 K in MCH, with the cross-section analysis at various points depicted as insets. The samples have been measured after vigorous shaking leading to mostly fractured bundles (left) and also single fibers (right). The samples have been spin-coated onto HOPG using a volume of 20 µL.

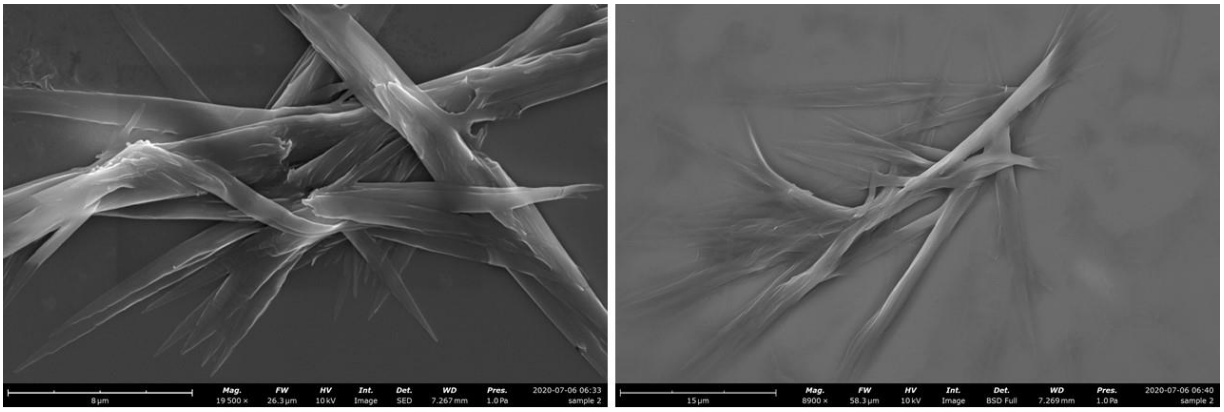

Figure S46: SEM images of **Agg2** recorded using a SED (left) and a BSD detector (right) with an acceleration voltage of 10 kV. The image sizes are 26.3 (left) and 58.3 µm (right) respectively. The samples were obtained after drop-casting roughly 10 µL of a solution of **2** in MCH (c = 2 x 10^{-5} M) onto a silicon wafer and subsequent Pt coating.

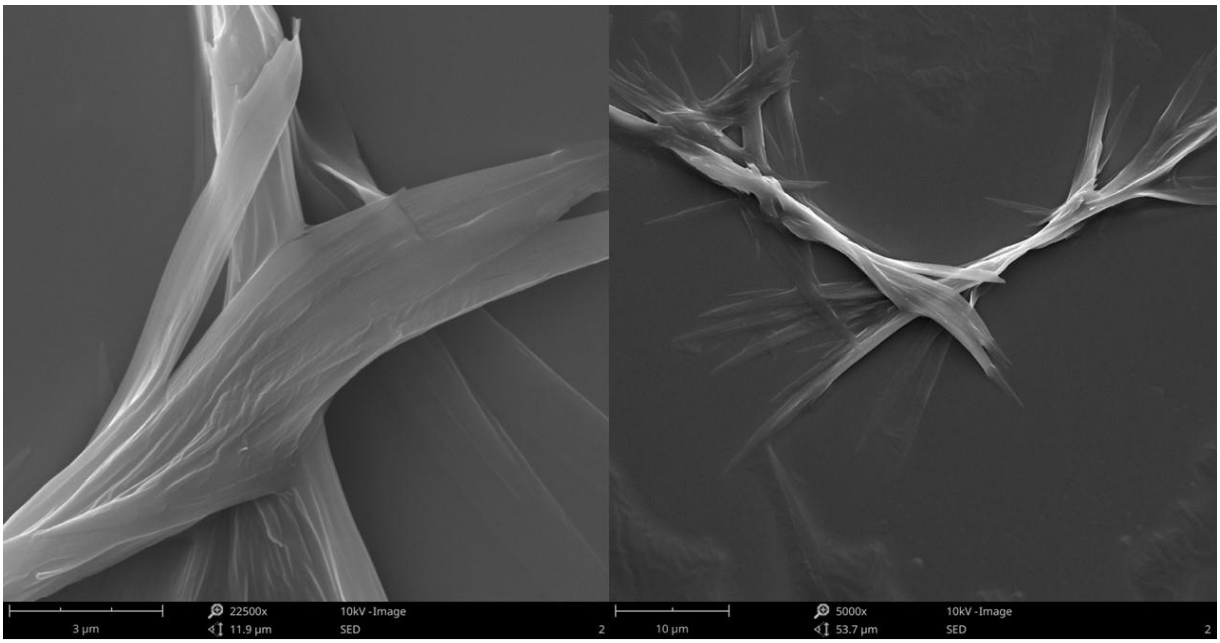

Figure S47: SEM images of **Agg2** recorded using a SED detector with an acceleration voltage of 10 kV. The image sizes are 11.9 (left) and 53.7 µm (right) respectively. The samples were obtained after drop-casting roughly 10 µL of a solution of **2** in MCH (c = 2 x 10^{-5} M) onto a silicon wafer and subsequent Pt coating.

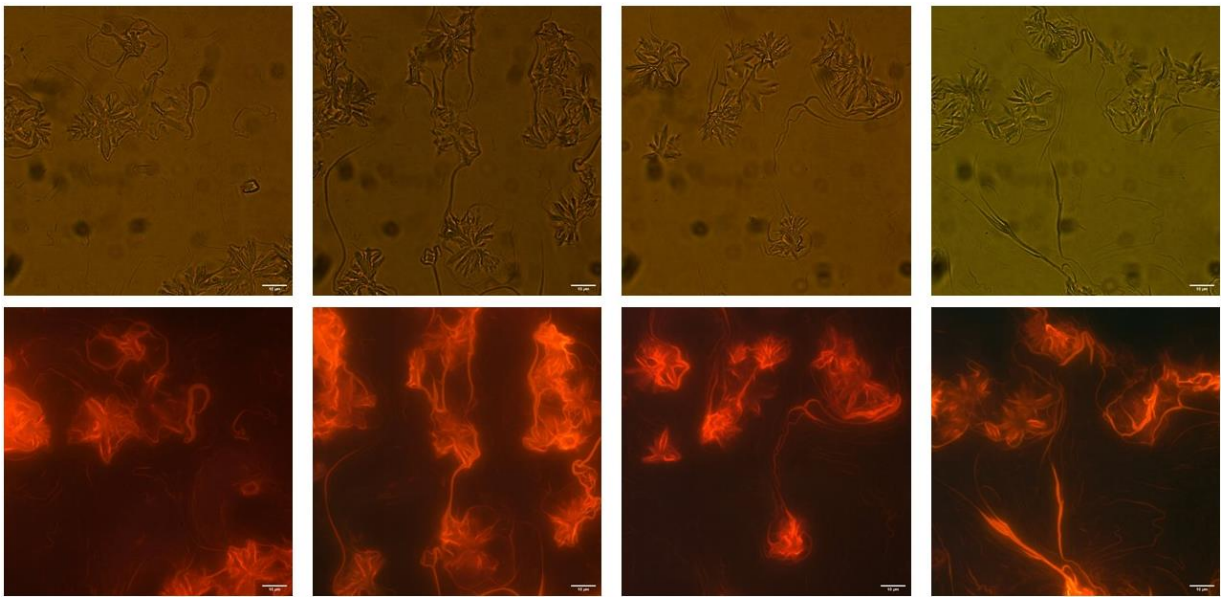

Figure S48: Micrograph (top) and luminescence micrograph (bottom) of **Agg1** (λ_{exc} = 375 nm).

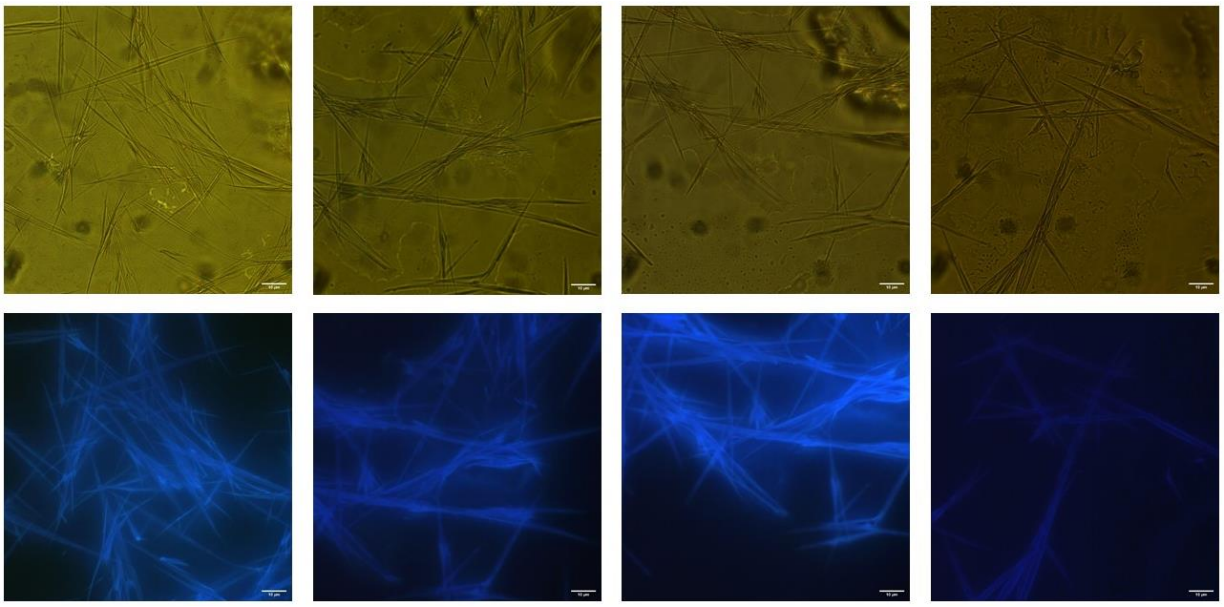

Figure S49: Micrograph (top) and luminescence micrograph (bottom) of **Agg2** (λ_{exc} = 375 nm).

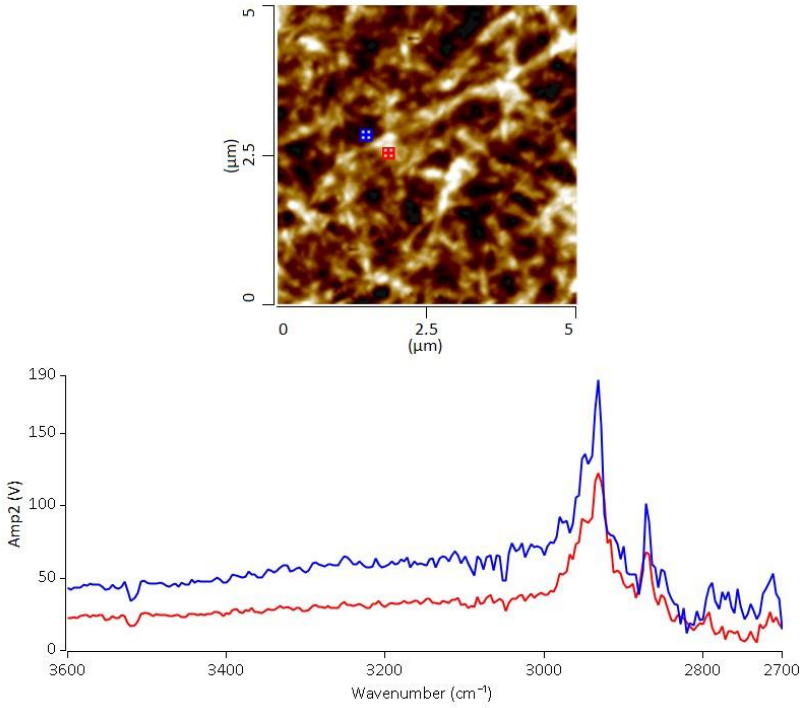

Figure S50: AFM height image of **Agg1** on Si-Wafer (top), with the IR spectra for different points on the surface depicted below.

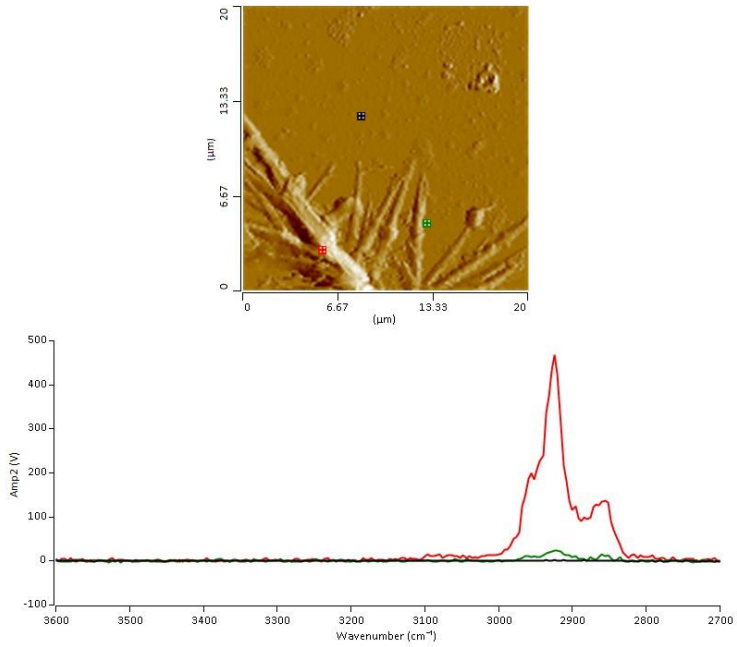

Figure S51: AFM Amplitude Error image of **Agg2** on Si-Wafer (note that the amplitude error image has been chosen to make the features corresponding to the green location on the surface more visible, top), with the IR spectra for different points on the surface depicted below.

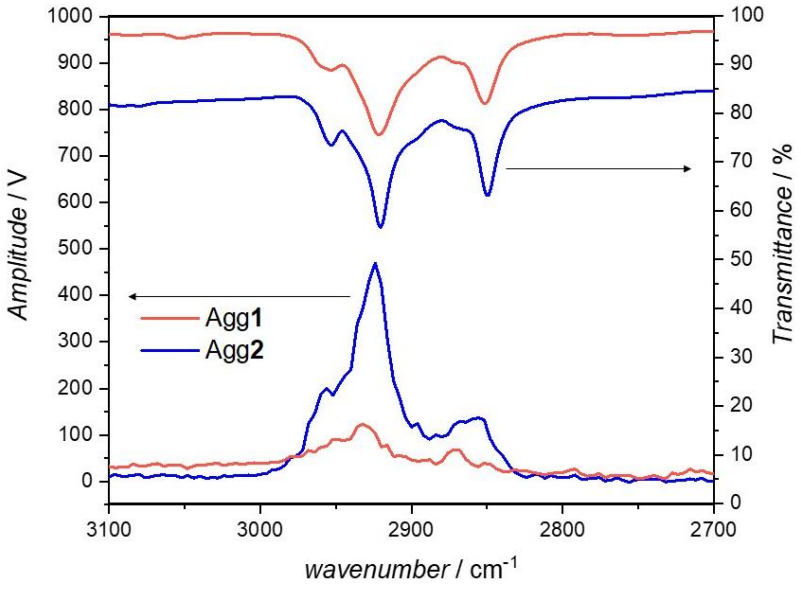

Figure S52: IR spectra of **Agg1** and **Agg2** in the thin film (top) and on surface (bottom) showing excellent agreement between both methods. Arrows indicate which y-axis is applicable.

The obtained results from conventional FT-IR of the thin films of **Agg1** and **Agg2** show an excellent match with the results obtained from Nano AFM-IR. Further, we can obtain more information on the surface of the polymer observed by conventional AFM. As the thin film analysis is devoid of any spatially resolved information, only very general conclusions can be drawn from this analysis. In comparison, Nano AFM-IR is able to allocate the observed characteristic interdigitation stretching bands to the polymers surface. This in-depth analysis allows correlation between conventional IR results and polymer surface chemistry. This pioneering introduction of Nano AFM-IR for the surface characterization of self-assembled metallosupramolecular polymers should encourage further surface characterization of self-assembled nanomaterials, which should aid the targeted development of functional materials.

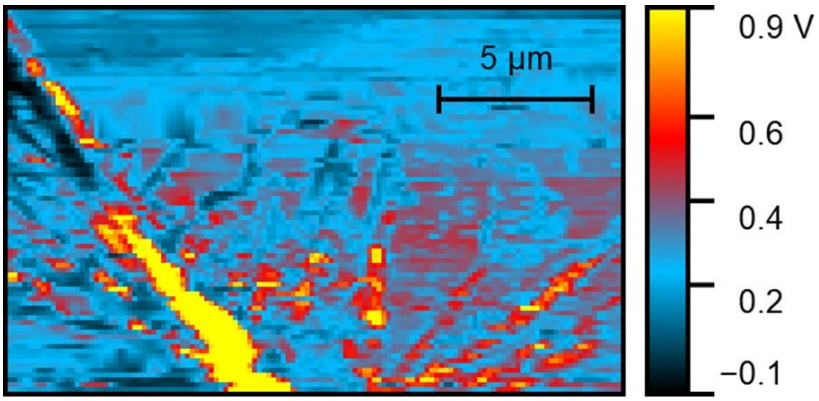

Figure S53: IR image of **Agg2** visualizing the IR absorbance of the alkyl shell of the aggregate at 2925 cm^{-1}.

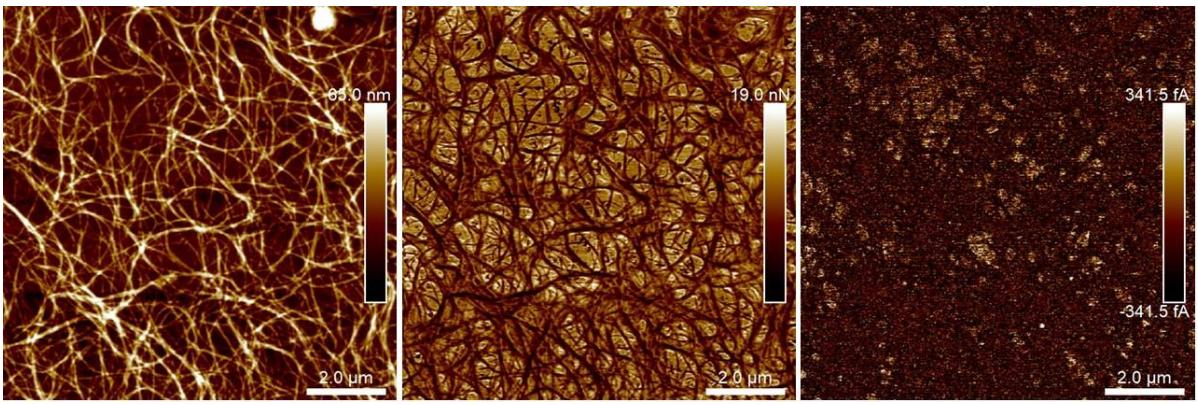

Figure S54: PF-TUNA measurement of **Agg1** on Si-Wafer including height (left), adhesion (middle) and contact current image (right, DC sample bias of 5 V).

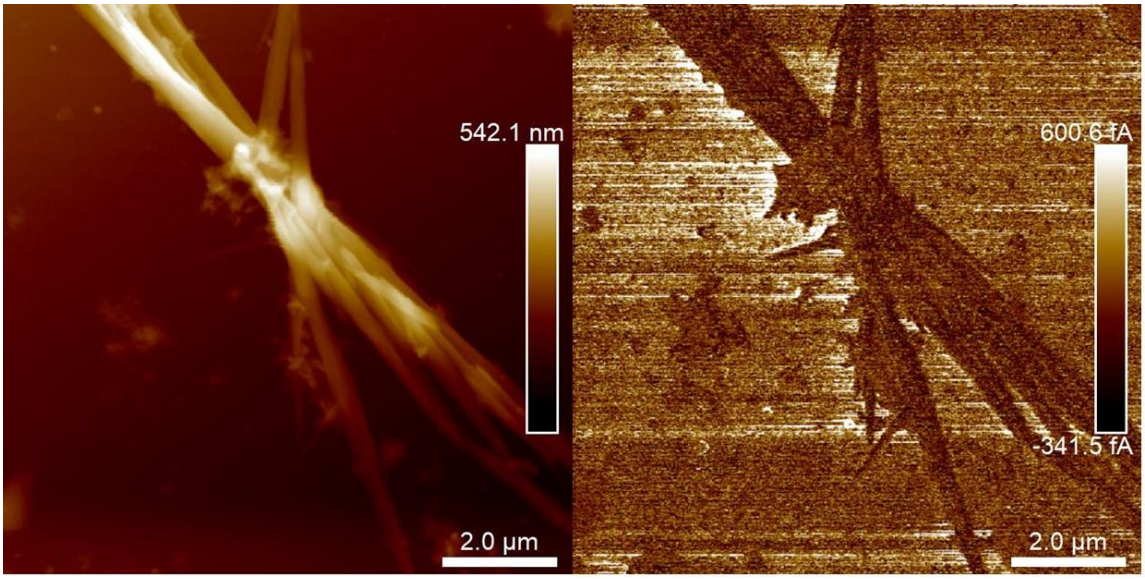

Figure S55: PF-TUNA measurement of **Agg2** on Si-Wafer including height (left) and contact current image (right, using a DC sample bias of 5 V).

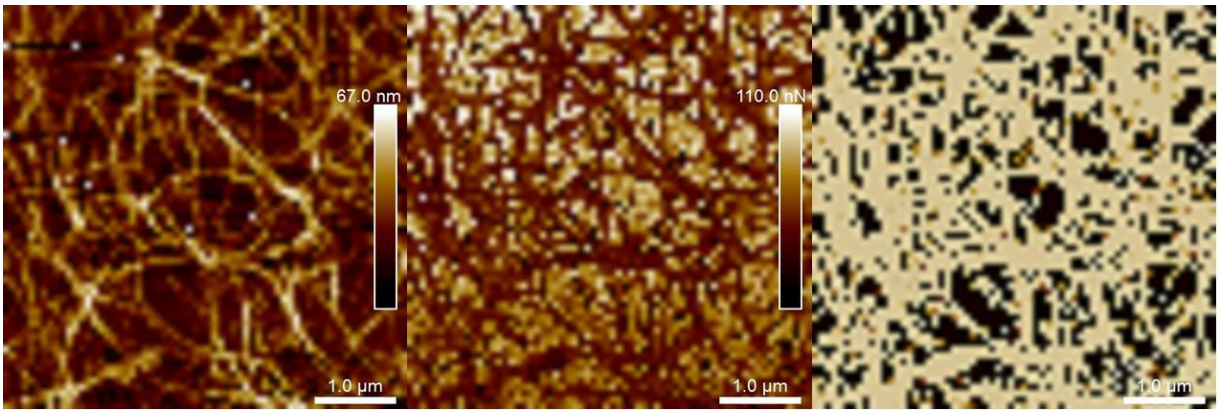

Figure S56: DCUBE-TUNA measurement of **Agg1** on Si-Wafer including height (left), adhesion (middle) and slice TUNA current image (right, color code: white: 93,8 pA, black: -177.9 pA, using a DC sample bias of 4.5 V).

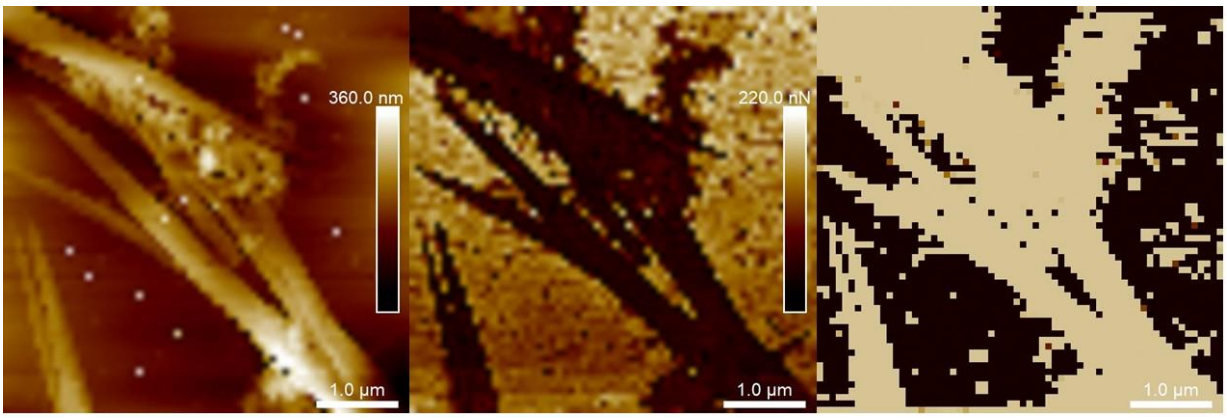

Figure S57: DCUBE-TUNA measurement of **Agg2** on Si-Wafer including height (left), adhesion (middle) and slice TUNA current image (right, color code: white: 124.9 pA, black: -152.1 pA, using a DC sample bias of 4.5 V).

4. References

(1) N. K. Allampally, A. Florian, M. J. Mayoral, C. Rest, V. Stepanenko, G. Fernández, H-aggregates of oligophenyleneethynylene (OPE)-BODIPY systems in water: guest size-dependent encapsulation mechanism and co-aggregate morphology. *Chem. Eur. J.,* 2014, **20**, 10669.

(2) V. R. L. J. Bloemendal, D. Sondag, H. Elferink, T. J. Boltje, J. C. M. van Hest, F. P. J. T. Rutjes. A Revised Modular Approach to (-)-trans-Δ8-THC and Derivatives Through Late-Stage Suzuki-Miyaura Cross-Coupling Reactions. *Eur. J. Org. Chem.,* 2019*, 2289.*

(3) M. Hosoyamada, N. Yanai, K. Okumura, T. Uchihashi, N. Kimizuka. Translating MOF chemistry into supramolecular chemistry: soluble coordination nanofibers showing efficient photon upconversion. *Chem. Commun*., 2018, **54**, 6828.

(4) L. Wu, M. Eberhart, B. Shan, A. Nayak, M. K. Brennaman, A. J. M. Miller, J. Shao, T. J. Meyer. Stable Molecular Surface Modification of Nanostructured, Mesoporous Metal Oxide Photoanodes by Silane and Click Chemistry. *ACS Appl. Mater. Interfaces,* 2019, ***11***, 4560.

(5) P. Moreno-García, M. Gulcur, D. Z. Manrique, T. Pope, W. Hong, V. Kaliginedi, C. Huang, A. S. Batsanov, M. R. Bryce, C. Lambert, et al. Single-molecule conductance of functionalized oligoynes: length dependence and junction evolution. *J. Am. Chem. Soc*., 2013, **135**, 12228.

(6) A. Langenstroer, K. K. Kartha, Y. Dorca, J. Droste, V. Stepanenko, R. Q. Albuquerque, M. R. Hansen, L. Sánchez, G. Fernández. Unraveling Concomitant Packing Polymorphism in Metallosupramolecular Polymers. *J. Am. Chem. Soc*., 2019, **141**, 5192.

(7) H. M. M. ten Eikelder, A. J. Markvoort, T. F. A. de Greef, P. A. J. Hilbers. An equilibrium model for chiral amplification in supramolecular polymers. *J. Phys. Chem. B,* 2012, **116**, 5291.

(8) N. K. Allampally, M. J. Mayoral, S. Chansai, M. C. Lagunas, C. Hardacre, V. Stepanenko, R. Q. Albuquerque, G. Fernández, *Chem. Eur. J.,* 2016, **22**, 7810.